Prepared for submission to JHEP

Light Primordial Black Holes from a First-Order Phase Transition near the End of Inflation: Baryogenesis and Gravitational Wave Signatures

Zihong Cheng[a] **Fa Peng Huang**[1a]

[a] *MOE Key Laboratory of TianQin Mission, TianQin Research Center for Gravitational Physics & School of Physics and Astronomy, Frontiers Science Center for TianQin, Gravitational Wave Research Center of CNSA, Sun Yat-sen University (Zhuhai Campus), Zhuhai 519082, China*

E-mail: chengzh83@mail2.sysu.edu.cn, huangfp8@sysu.edu.cn

arXiv:2611.08187v1 [hep-ph] 5 Nov 2026

Abstract: We investigate the formation and cosmological consequences of light primordial black holes (PBHs) from vacuum bubbles nucleated during a spectator sector first-order phase transition in inflation. We construct a phenomenological model in which the spectator potential evolves with the rolling inflaton, allowing vacuum bubbles to nucleate and grow during inflation. The vacuum ordering subsequently reverses near the end of inflation, leaving the bubble interiors in a metastable false vacuum state. We examine their stability against reverse vacuum tunneling and impose benchmark conditions to suppress this process before and after reheating. Sufficiently large bubbles can subsequently undergo supercritical evolution and form PBHs. In this framework, the PBH abundance is determined by the vacuum tunneling history, while the characteristic mass depends on the nucleation epoch and bubble growth during inflation. For sufficiently light PBHs that evaporate before big bang nucleosynthesis, Hawking radiation can create locally superheated regions in which electroweak symmetry is restored, potentially generating a baryon asymmetry in the presence of additional CP-violating interactions. We also investigate the direct gravitational wave (GW) signals from Hawking radiation and the induced GWs from PBH density fluctuations, the latter arising if an early PBH dominated epoch occurs. For representative benchmark parameters, the resulting baryon asymmetry can reach the ten-percent level of the observed value, while the induced GW signal can reach a peak amplitude of $\Omega_{\mathrm{GW},0}h^2 \sim 10^{-7}$ at frequencies of order 10–10^2 Hz.

Keywords: Phase Transitions in the Early Universe, Black Holes, Baryo-and Leptogenesis, Early Universe Particle Physics

[1]Corresponding author.

Contents

1 Introduction **2**

2 Spectator Sector Phase Transition during Inflation **5**
- 2.1 Spectator sector model and vacuum structure 6
- 2.2 Vacuum tunneling during inflation 9
- 2.3 Bubble nucleation rate and source distribution 9
- 2.4 Vacuum structure at the end of inflation and stability of the bubble interior 10

3 PBH Formation from Bubbles **11**
- 3.1 Inflationary evolution and bubble size 11
- 3.2 Horizon re-entry and supercritical bubble evolution 13
- 3.3 PBH mass and abundance 15
- 3.4 Monochromatic approximation 16

4 Hawking Evaporation and Cosmological Evolution **18**
- 4.1 Hawking evaporation 18
- 4.2 Radiation and entropy evolution 19

5 Electroweak Symmetry Restoration and Baryogenesis from Hawking Radiation of Light PBHs **21**
- 5.1 Landau–Pomeranchuk–Migdal thermalization and the explosive stage 21
- 5.2 Local electroweak symmetry restoration 22
- 5.3 Sphaleron window for baryogenesis 23
- 5.4 Baryon asymmetry 23

6 GW Signatures **26**
- 6.1 GWs from Hawking radiation 26
- 6.2 GWs induced by PBH density fluctuations 27

7 Numerical Results **29**

8 Conclusions **35**

A Vacuum Decay and Stability at the End of Inflation **37**
- A.1 CDL tunneling during inflation 37
- A.2 Shifted Potential at the End of Inflation 39
- A.3 Vacuum Decay before Reheating 39
- A.4 Post-reheating zero temperature bounce 41

B Spectator Potential Parameters for the Benchmark Points **43**

1 Introduction

First-order phase transitions (FOPTs) [1–4] in the early Universe can provide mechanisms for dark matter production in different forms, including nonthermally produced dark sector particles [5–12] and primordial black holes (PBHs) [13–22]. PBHs are themselves well-motivated dark matter candidates and can contribute to the dark matter abundance over phenomenologically allowed mass ranges [23, 24]. Depending on the nature of the transition and the dynamics of vacuum bubbles, PBH formation associated with FOPTs can proceed through several different channels, including bubble collisions [13–15] and the collapse of false vacuum regions [16–18, 22].

The possibility of forming wormholes and PBHs from vacuum bubbles was explored in early studies of cosmological FOPTs [25–27]. A distinct possibility, of particular relevance to the present work, is PBH formation from vacuum bubbles nucleated during inflation, as discussed in Ref. [28] and further developed in subsequent studies [29–34]. During inflation, these bubbles can grow through both cosmic expansion and bubble wall propagation, potentially reaching superhorizon scales. Depending on their size, interior vacuum energy, and wall tension, their subsequent evolution can follow either a subcritical or a supercritical branch [29–31]. Subcritical bubbles may collapse to form black holes, although their evolution can be affected by shape fluctuations originating from quantum fluctuations at nucleation, which may lead to fragmentation [30]. In contrast, the interior of a supercritical bubble continues to inflate and becomes connected to the exterior through a wormhole, with a black hole observed in the parent universe. This branch is less sensitive to the shape fluctuations that can affect subcritical collapse [30]. We therefore focus on supercritical bubbles as a more robust channel for PBH formation. A spectator sector provides a suitable setting for this mechanism, as it can undergo nontrivial vacuum dynamics during inflation while remaining subdominant in the total energy density [11, 32]. Inflaton-dependent vacuum tunneling has also been investigated as a mechanism for generating a localized PBH mass spectrum [34]. In the present work, rather than considering PBHs as dark matter candidates, we focus on the formation of light PBHs and their cosmological implications, particularly baryogenesis and gravitational wave (GW) signatures associated with their evaporation. We also examine the stability of the metastable bubble interiors against reverse vacuum tunneling before and after reheating.

To realize this mechanism, we construct a phenomenological model in which the rolling inflaton changes the effective spectator mass and hence the ordering of the spectator vacua. Before the transition, the spectator field s preferentially occupies the vacuum at $s = 0$. Around $N \simeq N_\star$, the nonzero minimum becomes lower in energy, allowing Coleman–De Luccia (CDL) vacuum tunneling [35, 36] and the nucleation of bubbles of the nonzero phase. These bubbles can subsequently expand while the nonzero phase remains energetically favored. As inflation proceeds toward its end, the vacuum ordering reverses, leaving the bubble interiors in a positive energy metastable state. This introduces an important consistency requirement for subsequent PBH formation: reverse vacuum tunneling inside these bubbles must remain sufficiently suppressed, particularly after reheating when the bubbles can still be superhorizon. We take this requirement into account by imposing

benchmark stability conditions on the metastable interior before and after reheating. Provided that these conditions are satisfied, sufficiently large bubbles can undergo supercritical evolution and form PBHs. In this framework, the PBH abundance is determined by the vacuum tunneling history, while the characteristic mass is controlled by the nucleation epoch and the bubble growth history during inflation, with the accumulated wall propagation parameterized by $v_{\rm eff}$. Both quantities are thus linked to the underlying spectator sector dynamics rather than introduced as independent phenomenological inputs.

The critical mass separating the subcritical and supercritical regimes depends on the characteristic scales of the bubble and can vary over a broad range as the underlying model parameters are changed [29], leaving open the possibility of forming sufficiently light PBHs in the supercritical regime. The subsequent Hawking evaporation of such PBHs [37–39] can have important consequences for the early Universe. In particular, Hawking radiation can provide a nonthermal source of dark matter particles [40–43], while entropy injection from PBH evaporation can dilute a pre-existing baryon asymmetry [44]. The energy deposited by Hawking radiation can also create localized hot spots, potentially affecting dark matter production and baryogenesis [45]. Independently of evaporation, pre-existing PBHs may modify vacuum bubble nucleation during FOPTs through their gravitational effects [46].

Of particular interest to the present work is baryogenesis during the final explosive stage of PBH evaporation [47]. Energetic Hawking radiation deposits energy into the surrounding plasma and can create a locally superheated region in which electroweak symmetry is restored [48]. If the PBH explosions occur after sphaleron processes [49, 50] have become inefficient in the ambient plasma, baryon number generated at the moving interfaces of this region may survive subsequent washout in the presence of additional CP-violating interactions. The resulting baryon asymmetry depends on the PBH abundance, the entropy produced during evaporation, and the thermal and hydrodynamic conditions at the final explosive stage.

The same PBH population can also generate GWs through two physically distinct mechanisms. Gravitons are emitted directly through Hawking radiation, producing a stochastic GW background extending to very high frequencies [51, 52]. In addition, if the PBH population becomes dynamically dominant before evaporation, fluctuations in the PBH number density can source scalar perturbations and subsequently induce GWs at second order [42, 53–55]. The direct Hawking component is determined by the evaporation history of the PBHs, whereas the density fluctuation contribution depends strongly on the PBH abundance and on the existence of an intermediate PBH dominated epoch.

In this work, we investigate these phenomena within a single spectator sector FOPT during inflation. Figure 1 illustrates the sequence from the inflaton-driven evolution of the spectator potential to bubble nucleation, expansion, and subsequent PBH formation, together with the resulting baryogenesis and GW signatures. We determine the vacuum tunneling history and the resulting bubble population, follow the bubble growth and subsequent supercritical evolution, and derive the corresponding PBH mass and abundance from the spectator sector parameters and the phenomenological bubble growth prescription. We then study the Hawking evaporation of the resulting PBH population, including its effects on the radiation and entropy evolution, and calculate the baryon asymmetry gen-

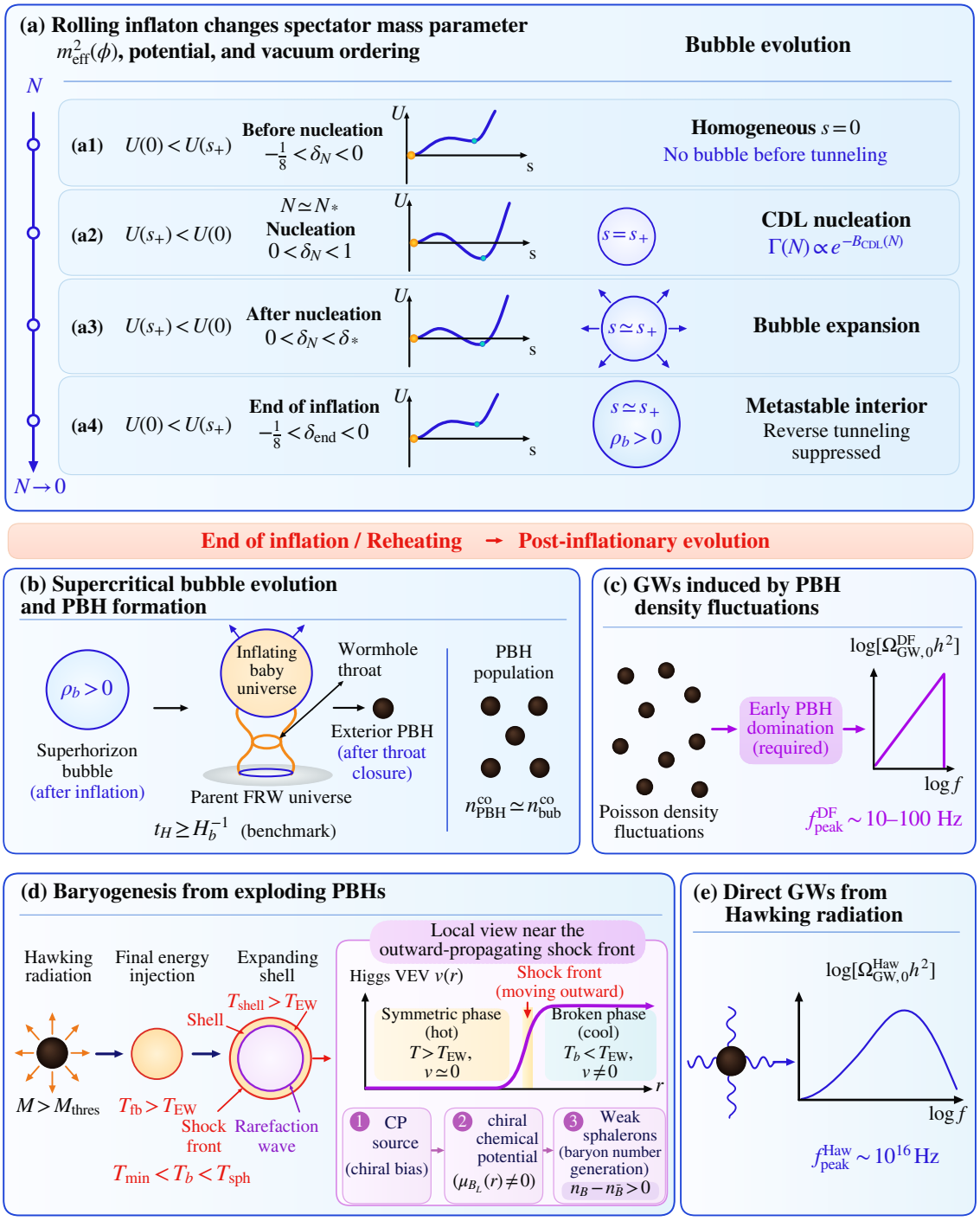


Figure 1: Schematic overview of PBH formation from a spectator sector FOPT during inflation and its subsequent cosmological signatures. (a) Four representative stages of the inflaton-driven evolution of the potential, vacuum ordering, and bubble dynamics of the spectator scalar field s. Initially, the $s = 0$ vacuum is energetically favored. Near $N \simeq N_\star$, the nonzero field minimum becomes the lower energy state, allowing CDL tunneling [35, 56] and the nucleation of bubbles that subsequently expand during inflation. As the inflaton evolves away from the nucleation epoch, the vacuum ordering eventually reverses, rendering the bubble interiors energetically disfavored. The

resulting reversal of the vacuum pressure opposes the outward motion of the bubble walls and, together with wall tension and Hubble damping, can gradually decelerate their expansion [31, 57]. By the end of inflation, the bubble interiors are assumed to remain in a positive energy metastable false vacuum state. (b) Post-inflationary evolution of a supercritical vacuum bubble. In the supercritical regime, an inflating interior develops behind a wormhole throat connecting it to the parent spacetime. The eventual closure of the throat leaves a PBH in the exterior region [29, 30]. (c) GWs induced by Poisson fluctuations in the PBH number density, provided that an early PBH dominated epoch occurs [53]. (d) Baryogenesis during the final explosive stage of PBH evaporation. Energy deposition from Hawking radiation drives an expanding shock and creates a locally electroweak symmetric region. The enlarged view near the outward-propagating shock front illustrates the Higgs vacuum expectation value profile and the roles of CP-violating sources, chiral chemical potentials, and weak sphaleron processes in baryon number generation [47, 48]. (e) GWs originating from direct graviton emission through Hawking radiation [51]. This figure was created with the assistance of OpenAI.

erated during the final explosive stage. We further investigate the GW signals from direct Hawking graviton emission and PBH density fluctuations. A central feature of our scenario is that the PBH mass and initial abundance are linked to the bubble nucleation and growth history during inflation and the vacuum tunneling history, respectively, rather than specified independently. These quantities provide the initial conditions for the subsequent baryogenesis and GW phenomenology.

For the representative viable parameter points considered in this work, the resulting PBHs have characteristic masses in the range $\mathcal{O}(10^5)$–$\mathcal{O}(10^6)\,\mathrm{g}$. For the benchmark CP-violating scale $\Lambda = 1$ TeV, the normalized baryon yield can reach $\mathcal{O}(10^{-1})$ of the observed baryon asymmetry. The GW signal induced by PBH density fluctuations (DF) can reach a peak amplitude of $\Omega_{\mathrm{GW},0}^{\mathrm{DF,peak}} h^2 \sim 10^{-7}$ at frequencies of order 10–$10^2\,\mathrm{Hz}$, whereas the GW contribution from direct Hawking radiation peaks at much higher frequencies. These results illustrate how a single spectator sector phase transition during inflation can connect PBH formation with baryogenesis and GW signatures.

The remainder of this paper is organized as follows. In Sec. 2, we introduce the spectator sector model and study the FOPT and vacuum tunneling during inflation. In Sec. 3, we discuss the evolution of the nucleated bubbles and derive the resulting PBH mass and abundance. In Sec. 4, we describe Hawking evaporation and the associated cosmological evolution. In Sec. 5, we study baryogenesis from the final explosive stage of PBH evaporation. The associated GW signatures are discussed in Sec. 6, and the numerical results are presented in Sec. 7. We conclude in Sec. 8. In Appendix A, we provide further details on vacuum decay and stability during and after inflation. Appendix B lists the spectator potential parameters for the benchmark points considered in our numerical analysis.

2 Spectator Sector Phase Transition during Inflation

In this section, we introduce the spectator sector model and study the vacuum transition that occurs during inflation. The time dependence of the mass parameter of the spectator scalar field s creates a finite interval during which the nonzero minimum becomes energetically favored over the vacuum at $s = 0$, allowing vacuum tunneling and bubble nucleation to

take place. The nucleated bubbles subsequently evolve during inflation, with their physical size affected by both the cosmic expansion and the propagation of the bubble wall. As the spectator mass parameter returns toward its post transition value, the ordering of the two vacua is reversed: the vacuum at $s = 0$ again becomes the global minimum, while the field inside the bubbles is assumed to remain near the nonzero local minimum, which becomes metastable. The positive vacuum energy retained inside these bubbles then provides the interior vacuum energy scale relevant for the subsequent supercritical evolution discussed in Sec. 3. The corresponding evolution of the spectator potential and bubble dynamics is illustrated schematically in Fig. 1(a).

2.1 Spectator sector model and vacuum structure

We consider an inflationary scenario involving the inflaton ϕ and a spectator scalar field s, with the total potential given by

$$V(\phi, s) = V_{\rm inf}(\phi) + U(s; \phi), \tag{2.1}$$

where ϕ is the inflaton and s denotes a spectator scalar field. The spectator contribution is assumed to remain subdominant throughout the relevant stage of inflation,

$$|U(s; \phi)| \ll V_{\rm inf}(\phi), \tag{2.2}$$

so that the background expansion is controlled by the inflaton sector. We take the spectator potential to be

$$U(s; \phi) = \frac{1}{2} m_{\rm eff}^2(\phi) s^2 - \frac{b}{3} s^3 + \frac{\kappa}{4} s^4, \qquad b > 0, \qquad \kappa > 0. \tag{2.3}$$

Field-dependent masses $m_{\rm eff}$ can arise when scalar fields are coupled to a rolling background field. In particular, when a scalar field evolves through special regions in field space, such as enhanced symmetry points, additional degrees of freedom can become light and be produced nonadiabatically [58–60]. The backreaction of the produced particles can significantly affect the dynamics of the inflaton and provide an additional source of friction during inflation [58, 61, 62].

Motivated by these mechanisms, we consider an inflaton-dependent mass for the spectator field whose variation becomes significant over a finite interval of the inflationary trajectory. In contrast to trapped-inflation scenarios, we do not rely on particle production backreaction to control the inflationary dynamics. Since the inflaton potential is not specified explicitly in the present setup, we assume that the inflaton continues to evolve through the relevant field range without becoming trapped.

Any spectator particles produced by the nonadiabatic evolution of the mass parameter are assumed to decay into lighter dark sector states. As discussed in Ref. [58], decay or annihilation of the produced particles reduces their number density and can thereby weaken the trapping effect associated with their backreaction. We assume that the decay dynamics lies in a regime in which the spectator particle population is sufficiently depleted for the inflaton to continue evolving through the relevant field range, while the total energy

density carried by the produced spectator particles and their dark sector decay products remains subdominant,

$$\rho_{\delta s} + \rho_D \ll 3M_{\rm Pl}^2 H_i^2. \tag{2.4}$$

The precise condition for satisfying these requirements depends on the particle production and decay processes as well as on the inflaton potential and the interactions between the inflaton and spectator sectors [58, 61, 62]. Since we do not specify the inflaton potential or a complete microscopic realization of these interactions, a quantitative analysis of this condition is beyond the scope of the present work and is left for future study.

We adopt the following phenomenological parametrization:

$$m_{\rm eff}^2(\phi) = m_0^2 - \Delta m^2 \exp\left[-\frac{(\phi-\phi_\star)^2}{2\sigma_\phi^2}\right]. \tag{2.5}$$

Here m_0^2 denotes the baseline value of the spectator mass parameter, while Δm^2 controls the amplitude of its variation around $\phi = \phi_\star$.

We parameterize the inflationary trajectory by the number of e-folds before the end of inflation,

$$N(t) = \int_t^{t_{\rm end}} H(t')\, dt', \qquad \frac{dN}{dt} = -H. \tag{2.6}$$

Over the relevant inflationary interval, we assume a slowly varying Hubble rate, such that $H(N) \simeq H_\star \simeq H_i$. Following Ref. [11], we parameterize the inflaton evolution during the relevant stage of inflation in terms of the number of e-folds, with $\phi(N) \simeq N M_{\rm Pl}\sqrt{2\bar{\epsilon}_V}$ under the slow-roll approximation. We then describe the corresponding evolution of the spectator mass parameter as

$$m^2(N) = m_0^2 - \Delta m^2 \exp\left[-\frac{(N-N_\star)^2}{2\sigma_N^2}\right], \tag{2.7}$$

where $N_\star$ specifies the center of the Gaussian profile and σ_N characterizes its width in e-fold space. Using the slow-roll relation between the inflaton field and the number of e-folds, the corresponding width in field space is

$$\sigma_\phi \simeq \sqrt{2\bar{\epsilon}_V}\, M_{\rm Pl}\sigma_N. \tag{2.8}$$

The evolution of $m^2(N)$ changes the relative depths of the two minima of the spectator potential. To characterize the resulting vacuum structure, we first note that the two minima become degenerate at

$$m_{\rm deg}^2 = \frac{2b^2}{9\kappa}. \tag{2.9}$$

It is convenient to introduce the dimensionless parameters

$$\alpha_0 \equiv \frac{m_0^2}{m_{\rm deg}^2}, \qquad \delta_m \equiv \frac{\Delta m^2}{m_{\rm deg}^2}, \tag{2.10}$$

together with

$$\delta_N \equiv 1 - \frac{m^2(N)}{m_{\rm deg}^2} = 1 - \alpha_0 + \delta_m \exp\left[-\frac{(N-N_\star)^2}{2\sigma_N^2}\right]. \tag{2.11}$$

At fixed N, the stationary points of the spectator potential satisfy

$$\frac{\partial U_N}{\partial s} = s\left[m^2(N) - bs + \kappa s^2\right] = 0. \tag{2.12}$$

Besides the stationary point at $s = 0$, the two nonzero stationary points are

$$s_{\pm,N} = \frac{b}{6\kappa}\left(3 \pm \sqrt{1 + 8\delta_N}\right), \tag{2.13}$$

where $s_{+,N}$ is the nonzero local minimum and $s_{-,N}$ is the barrier top. The nonzero extrema exist for

$$\delta_N > -\frac{1}{8}. \tag{2.14}$$

The relative vacuum energies are controlled by δ_N. For $\delta_N > 0$, the nonzero minimum has a lower vacuum energy than the $s = 0$ configuration. In the range

$$0 < \delta_N < 1, \tag{2.15}$$

the $s = 0$ configuration remains a local minimum and can therefore decay to the nonzero phase through bubble nucleation. In contrast, for

$$-\frac{1}{8} < \delta_N < 0, \tag{2.16}$$

the $s = 0$ phase is the true vacuum, while the nonzero minimum remains as a positive energy metastable state. At the center of the Gaussian profile, $N = N_\star$, we define

$$\delta_\star \equiv \delta_{N_\star} = 1 - \alpha_0 + \delta_m. \tag{2.17}$$

For the desired vacuum transition, we require $0 < \delta_\star < 1$, such that the vacuum at $s = 0$ remains a local minimum while the nonzero minimum becomes energetically favored. Vacuum tunneling from the vacuum at $s = 0$ to the nonzero minimum can therefore occur around $N = N_\star$.

By the end of inflation, $N = 0$, the mass parameter has evolved back toward its baseline value. We require $-1/8 < \delta_{\rm end} < 0$, such that the vacuum at $s = 0$ is again the global minimum, while the nonzero local minimum remains as a positive energy metastable state. We assume that the field inside the bubbles remains near this nonzero local minimum after the ordering of the two vacua is reversed. The bubbles nucleated during the earlier interval can therefore retain a metastable interior at the end of inflation.

Throughout this work, the spectator sector FOPT refers to this finite interval of vacuum tunneling and bubble nucleation during inflation. We do not require the phase transition to complete through the percolation of nucleated bubbles. Instead, we consider a dilute bubble population for which bubble overlap is negligible and whose subsequent evolution can lead to PBH formation.

2.2 Vacuum tunneling during inflation

We next determine the vacuum decay rate during the interval in which the nonzero phase is energetically favored. Since the spectator potential varies with the inflationary background, the tunneling problem is intrinsically time dependent. We adopt a quasi-static approximation in which the background value of ϕ, or equivalently N, is held fixed during each tunneling event.

At each fixed N, we treat the slowly varying spectator potential in Eq. (2.3), with the mass parameter specified by Eq. (2.7), quasi-statically and evaluate the CDL tunneling exponent using the semi-analytic treatment of quartic potentials in de Sitter space developed by Sasaki, Stewart, and Tanaka (SST) [56]. For our potential, the variables entering this treatment can be written as

$$B_{\rm CDL}(N) = \frac{\pi^2}{6\kappa}(1-\delta_N)\widetilde{B}_{\rm SST}\left[\varepsilon_{\rm SST}(N), \Omega_{\rm SST}(N)\right], \tag{2.18}$$

where the dimensionless variables and the fitting function $\widetilde{B}_{\rm SST}$ are summarized in Appendix A.

We focus on the parameter region in which the transition is described by a nonconstant CDL bounce rather than by Hawking–Moss transition. The curvature at the barrier top is

$$\mu^2_{\rm top}(N) \equiv -U''_N(s_{-,N}) = \frac{b^2}{18\kappa} q_N(3-q_N), \qquad q_N \equiv \sqrt{1+8\delta_N}, \tag{2.19}$$

and at the center of the nucleation feature we impose

$$\frac{\mu^2_{\rm top,\star}}{H_i^2} \gtrsim 4. \tag{2.20}$$

Together with the weak gravitational backreaction condition required for the quartic fit, Eq. (2.20) defines the region in which we use the CDL description.

The nucleation rate per unit physical four-volume is then written as [35, 63, 64]

$$\Gamma(N) = A_{\rm tun}(N)\exp[-B_{\rm CDL}(N)], \tag{2.21}$$

where $A_{\rm tun}$ denotes the fluctuation prefactor. For the numerical estimates below, we use $A_{\rm tun} \sim H_i^4$ as an order-of-magnitude normalization and retain the exponential dependence on the bounce action as the dominant source of the nucleation profile.

2.3 Bubble nucleation rate and source distribution

The time dependence of the spectator mass localizes vacuum tunneling around $N = N_\star$. In the parameter region of interest, the CDL exponent reaches its minimum near this point, and the corresponding nucleation rate is therefore sharply peaked within a finite interval.

To determine the resulting bubble abundance, we normalize the scale factor such that $a(t_{\rm end}) = 1$, which gives $a(N) = e^{-N}$ during inflation. For a unit comoving volume, the corresponding physical volume at the time of nucleation is $a^3(N)$. The number of bubbles nucleated during an interval dN is therefore

$$dn^{\rm co}_{\rm bub} = a^3(N)\Gamma(N)|dt| = a^3(N)\frac{\Gamma(N)}{H(N)}\,dN = \frac{e^{-3N}\Gamma(N)}{H(N)}\,dN, \tag{2.22}$$

where we have used $dN/dt = -H$. It follows that

$$\frac{dn_{\rm bub}^{\rm co}}{dN} = \frac{e^{-3N}\Gamma(N)}{H(N)}. \tag{2.23}$$

The total comoving number density of nucleated bubbles is therefore

$$n_{\rm bub}^{\rm co} = \int_{\rm source} dN\, \frac{e^{-3N}\Gamma(N)}{H(N)}. \tag{2.24}$$

For later convenience, we characterize the localized source by its peak quantities,

$$\Gamma_\star \equiv \Gamma(N_\star), \qquad H_\star \equiv H(N_\star), \tag{2.25}$$

and define an effective source width,

$$\Delta N_{\rm nuc} \equiv \int_{\rm source} dN\, e^{-3(N-N_\star)}\, \frac{H_\star}{H(N)}\, \frac{\Gamma(N)}{\Gamma_\star}. \tag{2.26}$$

The total comoving bubble number density can then be written as

$$n_{\rm bub}^{\rm co} = e^{-3N_\star}\, \frac{\Gamma_\star}{H_\star} \Delta N_{\rm nuc}. \tag{2.27}$$

Here, $\Delta N_{\rm nuc}$ denotes the effective width of the nucleation interval, with the N dependence of the factor e^{-3N} and of the Hubble rate included in its definition.

Since the nucleation rate is localized around $N_\star$, the resulting bubble population is also concentrated around a characteristic comoving scale. An approximately monochromatic PBH population is obtained when the corresponding variation of the PBH mass across the source interval is sufficiently small. We quantify this condition after deriving the relation between the nucleation time and the PBH mass in Sec. 3.

2.4 Vacuum structure at the end of inflation and stability of the bubble interior

As the spectator mass returns toward its baseline value near the end of inflation, the vacuum at $s = 0$ becomes the global minimum again, while the nonzero local minimum remains present for $-1/8 < \delta_{\rm end} < 0$, as discussed in Sec. 2.1. For the subsequent evolution, we focus on the regime in which the field configuration inside a nucleated bubble remains sufficiently close to the nonzero local minimum, $s_{\rm in,end} \simeq s_{+,\rm end}$. The bubble interior therefore corresponds to a metastable vacuum with positive energy density. The associated vacuum energy density is

$$\rho_b = \frac{b^4}{5184\kappa^3}(1 - q_{\rm end})(3 + q_{\rm end})^3, \qquad q_{\rm end} = \sqrt{1 + 8\delta_{\rm end}}, \tag{2.28}$$

which defines the corresponding interior de Sitter scale,

$$H_b^2 = \frac{\rho_b}{3M_{\rm Pl}^2}. \tag{2.29}$$

For the bubbles to survive and subsequently undergo the supercritical evolution discussed in Sec. 3, reverse vacuum tunneling from their metastable interiors to the true vacuum must remain sufficiently suppressed. During the remaining inflationary evolution, we estimate its decay in the quasi-de Sitter background using the quartic vacuum decay treatment of Ref. [56]. After reheating, we assume that the spectator sector remains decoupled from the ambient radiation bath, so that thermal corrections to the spectator potential are negligible. The decay of the metastable interior can then be treated as a zero temperature $O(4)$ tunneling process, for which we use the quartic potential results of Ref. [65]. The corresponding bounce scales and the validity of the flat space approximation are discussed in Appendix A.

Rather than attempting a fully time-dependent calculation of the integrated decay probability, we impose conservative benchmark conditions requiring the vacuum decay evaluated at the end of inflation, $N = 0$, to be exponentially more suppressed than the tunneling process responsible for bubble production,

$$B_{\rm end}^{\rm dS} > B_\star + \Delta B_{\rm safe}, \qquad B_{4,\rm end}^{\rm flat} > B_\star + \Delta B_{\rm safe}, \qquad \Delta B_{\rm safe} \gg 1, \tag{2.30}$$

whenever the corresponding decay channel is physically applicable. These conditions are used as benchmark stability criteria and are not intended to replace a complete treatment of vacuum decay throughout the subsequent time-dependent background.

Together with the bubble source derived in Sec. 2.3, the vacuum configuration at the end of inflation, $N = 0$, determines the conditions relevant for the subsequent bubble evolution. The bubble source fixes the initial bubble population, while the metastable interior determines the positive vacuum energy stored inside the bubbles. In particular, Eq. (2.29) defines one of the characteristic scales entering the subsequent bubble dynamics. We now turn to the inflationary growth, horizon re-entry, and supercritical evolution of these bubbles, and to their eventual conversion into PBHs.

3 PBH Formation from Bubbles

The preceding section determines both the bubble source and the metastable vacuum energy stored in the bubble interior. We now follow the subsequent evolution of these bubbles, determine the condition for entering the supercritical regime, and map the inflationary nucleation history onto the PBH mass and abundance. For simplicity, we assume instantaneous reheating followed by radiation domination. The bubble wall evolution and the effects of the surrounding plasma are treated phenomenologically.

3.1 Inflationary evolution and bubble size

Consider a bubble nucleated at N e-folds before the end of inflation with physical radius $R_n(N)$. Since the scale factor is normalized by $a(t_{\rm end}) = 1$, the scale factor at nucleation is $a_n = e^{-N}$. The comoving bubble radius at the end of inflation can therefore be written as

$$\chi_i(N) = e^N R_n(N) + \int_{t_n}^{t_{\rm end}} \frac{v_w(t')}{a(t')}\, dt', \tag{3.1}$$

where v_w denotes the wall velocity relative to the Hubble flow. For an approximately constant inflationary Hubble rate H_i, we parameterize the integrated wall propagation by an effective velocity $v_{\rm eff}$ through

$$\int_{t_n}^{t_{\rm end}} \frac{v_w(t')}{a(t')}\, dt' \equiv \frac{v_{\rm eff}}{H_i}\left(e^N - 1\right). \tag{3.2}$$

The resulting scale is thus

$$\chi_i(N) = e^N R_n(N) + \frac{v_{\rm eff}}{H_i}\left(e^N - 1\right). \tag{3.3}$$

The bubble size at the end of inflation is therefore determined by both the cosmological expansion of its initial radius and the propagation of the bubble wall during inflation. Similar inflationary stretching of nucleated vacuum bubbles and their later evolution into compact objects have been studied in Ref. [29].

In this work, we consider the regime in which the second term in Eq. (3.3) dominates over the stretched nucleation radius,

$$e^N R_n(N) \ll \frac{v_{\rm eff}}{H_i}\left(e^N - 1\right), \tag{3.4}$$

so that

$$\chi_i(N) \simeq \frac{v_{\rm eff}}{H_i}\left(e^N - 1\right). \tag{3.5}$$

For the characteristic nucleation time $N = N_\star$, we denote $\chi_i \equiv \chi_i(N_\star)$. Since $a(t_{\rm end}) = 1$, this comoving scale is numerically equal to the physical bubble radius at the end of inflation. We further adopt, as a baseline approximation, that the characteristic comoving size of the bubble is determined predominantly during inflation.

The evolution of the bubble wall is expected to proceed through qualitatively different stages as the relative vacuum energies vary during inflation. Around the nucleation epoch, the nonzero minimum lies below the vacuum at $s = 0$, and the corresponding vacuum energy difference provides an outward volume pressure that drives the bubble wall away from the nucleation center. The wall can therefore acquire a sizable velocity during this stage, although its motion is simultaneously affected by the wall tension and curvature as well as by Hubble damping. As the spectator potential subsequently evolves and the vacuum ordering is reversed, the nonzero phase inside the bubble becomes the higher energy metastable vacuum. The vacuum pressure contribution then reverses sign and acts against the outward motion of the wall. Together with the curvature force and cosmological damping, this generically leads to a deceleration of the outward motion, as is familiar from the dynamics of biased domain walls and inflationary vacuum bubbles [31, 57].

In the parameter region considered here, however, the post-reversal vacuum bias cannot be arbitrarily large. In particular, the stability conditions imposed on the metastable bubble interior require its decay exponent at the end of inflation to be substantially larger than the exponent associated with the earlier bubble nucleation epoch. Within the present spectator potential, this requirement disfavors configurations with an excessively strong post-reversal vacuum energy splitting. Consequently, although the reversal of the vacuum

ordering provides a robust mechanism for decelerating an outward-moving wall, the deceleration need not be instantaneous and can occur over a finite interval of the inflationary evolution. The actual trajectory depends on the interplay of the evolving vacuum structure, the cosmological background, and the bubble wall dynamics. A quantitative determination therefore requires solving the full time-dependent wall equation of motion.

In the present phenomenological treatment, we do not attempt to resolve this detailed evolution. Instead, the accumulated wall propagation during inflation is encoded in the effective velocity $v_{\rm eff}$ introduced above. Motivated by the expected deceleration following the reversal of the vacuum ordering, we focus on the phenomenological regime in which the residual velocity is small by the end of inflation,

$$v_w(t_{\rm end}) \simeq 0. \tag{3.6}$$

This should be regarded as a phenomenologically motivated regime rather than as a first-principles prediction of the present analysis. Importantly, a small terminal velocity does not imply a small $v_{\rm eff}$: the latter measures the integrated displacement of the wall over the entire inflationary interval and can therefore remain sizable if the bubble undergoes substantial outward propagation during the earlier stage. The change in the sign of the vacuum pressure, together with the additional damping effects discussed above, provides physical support for such a separation between the accumulated wall propagation and its residual velocity at the end of inflation.

Following the treatment of inflationary vacuum bubbles in Ref. [29], we characterize the subsequent evolution by the comoving scale associated with the bubble size at the end of inflation. With instantaneous reheating and the normalization $a(t_{\rm end}) = 1$, this scale is simply χ_i, which is equal to the physical bubble radius at the end of inflation. We therefore use χ_i as the reference comoving scale for determining the horizon re-entry time. This prescription is consistent with the phenomenological regime adopted here, in which the residual motion of the wall is already small at the end of inflation, so that the leading contribution to the subsequent horizon-entry scale is set by the bubble size accumulated during inflation. A fully self-consistent treatment of the time-dependent wall dynamics, including the evolution of the spectator potential, gravitational effects, and the transition through reheating, is left for future work.

3.2 Horizon re-entry and supercritical bubble evolution

After instantaneous reheating, we assume radiation domination with the Hubble rate matched to H_i at $a = 1$. The subsequent expansion is then described by

$$H(a) = H_i a^{-2}. \tag{3.7}$$

A bubble scale $\chi_i(N)$ re-enters the Hubble horizon when its physical size $a_H \chi_i(N)$ becomes equal to $H^{-1}(a_H)$. Using Eq. (3.7), this gives

$$a_H(N) = H_i \chi_i(N). \tag{3.8}$$

For the re-entry to occur after reheating, the relevant source must satisfy $a_H \gtrsim 1$. The Hubble parameter at re-entry is consequently

$$H_{\rm form}(N) = \frac{H_i}{a_H^2(N)} = \frac{1}{H_i \chi_i^2(N)}, \tag{3.9}$$

and the corresponding Hubble time is

$$t_H(N) \equiv H_{\rm form}^{-1}(N) = H_i \chi_i^2(N). \tag{3.10}$$

We use t_H as the characteristic horizon re-entry time scale throughout.

Whether a re-entering vacuum bubble lies on the supercritical branch is not determined by the interior vacuum energy alone. In addition to the de Sitter scale H_b defined in Eq. (2.29), the wall tension introduces the gravitational scale [29–31]

$$H_\Sigma \equiv 2\pi G \Sigma, \tag{3.11}$$

where Σ is the wall tension. Following Ref. [29], the critical mass separating the subcritical and supercritical bubble regimes is parametrically determined by the interior de Sitter scale and the gravitational scale associated with the wall tension,

$$G M_{\rm cr} \sim \min\left\{H_b^{-1}, H_\Sigma^{-1}\right\}, \tag{3.12}$$

up to factors of order unity [29]. Above this critical scale, the bubble can enter the supercritical regime, in which the false vacuum interior continues to inflate and a black hole connected to the inflating interior through a wormhole is seen from the parent universe [29]. This evolution is illustrated schematically in Fig. 1(b).

During radiation domination, the horizon mass associated with a mode re-entering at N is

$$M_H(N) = \frac{4\pi}{3}\rho_{\rm rad}(N) H_{\rm form}^{-3}(N) = \frac{1}{2G H_{\rm form}(N)} = \frac{t_H(N)}{2G}. \tag{3.13}$$

Using the horizon-mass estimate in Eq. (3.13), the corresponding supercriticality condition can be written parametrically as [29–31]

$$t_H(N) \gtrsim \min\left\{H_b^{-1}, H_\Sigma^{-1}\right\}. \tag{3.14}$$

Since the criterion involving H_Σ is based on the thin-wall description, while some bubbles in our parameter space may lie outside the regime where the thin wall approximation is reliable, we do not use H_Σ as a universal benchmark. Instead, we adopt the phenomenological benchmark condition

$$t_H(N) \gtrsim H_b^{-1}, \tag{3.15}$$

which is sufficient to satisfy Eq. (3.14) since $\min\{H_b^{-1}, H_\Sigma^{-1}\} \leq H_b^{-1}$, but should not be interpreted as an exact necessary and sufficient criterion.

3.3 PBH mass and abundance

We now restrict our attention to bubbles satisfying the supercriticality condition discussed above. Following Ref. [29], we estimate the mass of the resulting PBH from the horizon mass associated with the corresponding re-entry scale. Using Eq. (3.13), this gives, up to factors of order unity,

$$M_{\rm PBH}(N) \simeq M_H(N) = \frac{t_H(N)}{2G} = \frac{H_i \chi_i^2(N)}{2G}. \tag{3.16}$$

In terms of the commonly used parametrization $M_{\rm PBH} = \gamma M_H$, where γ accounts for the order-one relation between the PBH mass and the horizon mass at formation, this prescription corresponds to setting $\gamma = 1$ [29–31]. We therefore do not introduce an additional collapse efficiency parameter. The supercriticality condition determines whether a bubble follows the supercritical branch, while the characteristic mass of the resulting PBH is estimated from the horizon scale associated with the bubble size acquired during inflation.

When the initial nucleation radius can be neglected, inserting Eq. (3.5) into Eq. (3.16) gives

$$M_{\rm PBH}(N) \simeq \frac{v_{\rm eff}^2}{2GH_i} \left(e^N - 1\right)^2. \tag{3.17}$$

Since the nucleation rate is concentrated around $N_\star$, the corresponding characteristic PBH mass is

$$M_\star \equiv M_{\rm PBH}(N_\star) \simeq M_H(N_\star) = \frac{H_i \chi_i^2}{2G} \simeq \frac{v_{\rm eff}^2}{2GH_i} \left(e^{N_\star} - 1\right)^2. \tag{3.18}$$

The associated Hubble time at horizon re-entry is

$$t_{H,\star} = H_{{\rm form},\star}^{-1} = H_i \chi_i^2 \simeq 2GM_\star. \tag{3.19}$$

Thus, within the approximations adopted here, both the characteristic PBH mass and the corresponding formation time scale are determined by the same bubble scale acquired during inflation.

The PBH abundance is inherited from the bubble nucleation history derived in Sec. 2.3. In the parameter region retained in our analysis, the bubbles contributing appreciably to the nucleation abundance satisfy the supercriticality condition, and we associate one exterior PBH with each such bubble. The resulting comoving PBH number density is therefore

$$n_{{\rm PBH},\star}^{\rm co} \simeq n_{\rm bub}^{\rm co} = e^{-3N_\star} \frac{\Gamma_\star}{H_\star} \Delta N_{\rm nuc}, \tag{3.20}$$

where $\Delta N_{\rm nuc}$ is defined in Eq. (2.26). At horizon entry,

$$a_{H,\star} = H_i \chi_i, \tag{3.21}$$

so that the physical PBH number density is

$$n_{{\rm PBH},\star}^{H} = \frac{n_{{\rm PBH},\star}^{\rm co}}{a_{H,\star}^3}. \tag{3.22}$$

The corresponding PBH-to-radiation energy density ratio is

$$\kappa_H^{\rm SB} \equiv \frac{\rho_{\rm PBH}^H}{\rho_{\rm rad}^H} \simeq \frac{n_{\rm PBH,\star}^{\rm co} M_\star}{a_{H,\star}^3 \left(3M_{\rm Pl}^2 H_{\rm form,\star}^2\right)}. \tag{3.23}$$

Here and throughout this work, the superscript or subscript "SB" stands for "spectator bubble" and labels quantities associated with the PBH population originating from the spectator sector phase transition. This ratio is a derived quantity rather than an independent normalization of the PBH abundance, which is fixed by the integrated tunneling history through Eq. (3.20).

The discussion above also provides physical motivation for the phenomenological prescriptions adopted throughout this subsection. In particular, the interior vacuum energy and the wall tension primarily control whether a bubble can enter the supercritical branch, whereas, once the bubble is sufficiently supercritical, the characteristic mass of the black hole seen from the exterior is governed predominantly by the cosmological horizon scale associated with the bubble size [29–31]. This behavior supports our use of the benchmark supercriticality criterion in Eq. (3.15) and the treatment in which the detailed wall microphysics enters mainly through the branch selection, while the bubble abundance is fixed by the tunneling history and the characteristic formation scale is determined by horizon re-entry. These prescriptions provide a consistent phenomenological description of the supercritical branch within the level of approximation adopted in the present analysis.

3.4 Monochromatic approximation

We emphasize that the quantity $\Delta N_{\rm nuc}$ introduced above is an effective width defined through the integrated nucleation abundance and should not be identified with the physical width of the nucleation interval relevant for the PBH mass distribution. We denote by $\Delta N_{\rm PBH}$ the range in N over which bubble nucleation contributes appreciably to the PBH population,

$$N \in [N_-, N_+], \qquad \Delta N_{\rm PBH} \equiv N_+ - N_-. \tag{3.24}$$

Within the mass mapping of Eq. (3.17), the masses associated with the two ends of this interval satisfy

$$\frac{M_{\rm max}}{M_{\rm min}} = \left[\frac{e^{N_+} - 1}{e^{N_-} - 1}\right]^2. \tag{3.25}$$

For the parameter region relevant to our analysis, nucleation occurs at $N \gg 1$, such that $e^N \gg 1$. Eq. (3.25) therefore reduces to

$$\frac{M_{\rm max}}{M_{\rm min}} \simeq e^{2(N_+ - N_-)} = e^{2\Delta N_{\rm PBH}}, \tag{3.26}$$

or equivalently,

$$\Delta \ln M_{\rm PBH} \equiv \ln \frac{M_{\rm max}}{M_{\rm min}} \simeq 2\Delta N_{\rm PBH}. \tag{3.27}$$

A localized PBH-producing nucleation history is compatible with the phenomenological bubble wall evolution adopted in Sec. 3.1. In particular, the condition $v_w(t_{\rm end}) \simeq 0$

constrains the residual velocity of the wall at the end of inflation, whereas $v_{\rm eff}$ characterizes the accumulated wall propagation over the preceding inflationary evolution. The spectator potential contains sufficient parametric freedom to vary the vacuum energy difference around the nucleation epoch and after the reversal of the vacuum ordering. A bubble can therefore acquire a sizable outward displacement during the earlier stage and subsequently decelerate over a finite interval without requiring the PBH-producing nucleation history itself to extend over the same interval. The corresponding freedom in the spectator potential is discussed further in Appendix B.

Within the phenomenological treatment adopted here, the post-reversal vacuum structure affects the subsequent wall evolution and the selection of the supercritical branch, but does not enter the PBH mass mapping directly. Once the accumulated propagation is parameterized by $v_{\rm eff}$, the characteristic mass in Eq. (3.17) is determined by the nucleation time, H_i, and $v_{\rm eff}$. Adjusting the vacuum energy difference after nucleation in order to realize a small residual wall velocity therefore does not by itself require a broad PBH mass distribution.

Moreover, the duration over which the spectator potential evolves need not coincide with the width of the nucleation history. The bubble source is controlled by

$$\frac{dn_{\rm bub}^{\rm co}}{dN} = \frac{e^{-3N}\Gamma(N)}{H(N)}, \tag{3.28}$$

with

$$\Gamma(N) \propto \exp[-B_{\rm CDL}(N)]. \tag{3.29}$$

Since the tunneling exponent develops a minimum around $N_\star$ in the parameter region of interest, the exponential dependence of the nucleation rate can localize the actual bubble source much more strongly than the underlying variation of the spectator potential [34]. A finite interval of potential evolution can therefore remain compatible with a substantially more localized nucleation history relevant for PBH production. This also explains why the width controlling the PBH mass distribution should be characterized directly by $\Delta N_{\rm PBH}$ rather than by the width of the spectator potential or by the effective abundance parameter $\Delta N_{\rm nuc}$.

Motivated by these considerations, we adopt as a phenomenological condition for the monochromatic-limit treatment

$$\Delta N_{\rm PBH} \lesssim 1. \tag{3.30}$$

This condition is independent of the benchmark choice $\Delta N_{\rm nuc} = 1$. From Eq. (3.26), it implies

$$\frac{M_{\rm max}}{M_{\rm min}} \lesssim e^2 \simeq 7.4, \tag{3.31}$$

or equivalently,

$$\Delta \ln M_{\rm PBH} \lesssim 2. \tag{3.32}$$

The PBHs contributing appreciably to the subsequent evolution are therefore confined to less than one decade in mass. In addition, within the present approximation the inflationary Hubble rate is slowly varying, the accumulated wall propagation is described by the

common parameter $v_{\rm eff}$, and the initial nucleation radius is neglected in the mass mapping. The dominant source of the PBH mass variation is therefore the finite range of nucleation times itself.

For the benchmark analysis below, we represent this localized PBH population by its characteristic mass $M_\star$ and adopt the monochromatic approximation,

$$\frac{dn^{\rm co}_{\rm PBH,i}}{dM_i} \simeq n^{\rm co}_{\rm PBH,\star}\delta\left(M_i - M_\star\right). \tag{3.33}$$

This prescription should be understood as the monochromatic-limit representation of a finite but localized PBH mass distribution. Possible effects associated with its residual finite width are discussed in Sec. 8.

4 Hawking Evaporation and Cosmological Evolution

The preceding section determines the characteristic PBH mass $M_\star$, the absolute comoving number density $n^{\rm co}_{\rm PBH,\star}$, and the scale factor $a_{H,\star}$ at horizon re-entry. We now follow the subsequent Hawking evaporation of this nearly monochromatic PBH population and its impact on the cosmological background. Throughout this section, we retain the global normalization $a(t_{\rm end}) = 1$ introduced in Sec. 3, without rescaling the scale factor at PBH formation. We take the horizon re-entry of the characteristic bubble scale as the initial epoch of the subsequent evolution and denote the elapsed time from this epoch by Δt.

4.1 Hawking evaporation

We consider uncharged and nonrotating PBHs. The Hawking temperature of a Schwarzschild black hole of mass M is [66]

$$T_H(M) = \frac{1}{8\pi GM} = \frac{M_{\rm Pl}^2}{M}. \tag{4.1}$$

As the PBH evaporates, its mass decreases and its Hawking temperature rises, leading to an increasingly rapid energy loss. For the mass range relevant to the baryogenesis mechanism considered here, $M_{\rm PBH} \lesssim 10^8\,{\rm g}$, one has $T_H \gtrsim 10^5\,{\rm GeV}$, so that all Standard Model particle species can be efficiently emitted [47, 48]. We therefore adopt the high temperature approximation used in Refs. [47, 48], for which the total Hawking mass loss rate is

$$-\frac{dM}{dt} = \frac{\mathcal{A}_{\rm evap} f_{\rm max}}{M^2}, \qquad \mathcal{A}_{\rm evap} = 6.04\times 10^{72}\,{\rm GeV}^4, \qquad f_{\rm max} = 15.52. \tag{4.2}$$

Here $f_{\rm max}$ is the limiting value of the Page factor [67] when all Standard Model degrees of freedom are kinematically accessible. Since the PBHs studied in this work remain well within the regime in which this approximation applies, we take $f(M) \simeq f_{\rm max}$ throughout the subsequent evaporation calculation.

For later convenience, we define $\mathcal{A}_f \equiv \mathcal{A}_{\rm evap} f_{\rm max}$. For the monochromatic population in Eq. (3.33), all PBHs are formed with the same initial mass $M_\star$. Measuring the elapsed time from horizon re-entry by Δt, with $\Delta t = 0$ at this epoch, integration of Eq. (4.2) gives

$$M(\Delta t) = \left(M_\star^3 - 3\mathcal{A}_f \Delta t\right)^{1/3}, \qquad 0 \le \Delta t < \tau_\star, \tag{4.3}$$

where

$$\tau_\star = \frac{M_\star^3}{3\mathcal{A}_f} \tag{4.4}$$

is the evaporation lifetime. Numerically,

$$\tau_\star \simeq 4.14 \times 10^{-10}\,\mathrm{s} \left(\frac{M_\star}{10^6\,\mathrm{g}}\right)^3, \tag{4.5}$$

in agreement with Ref. [47, 48]. The strong increase of the Hawking emission rate during the final stage of evaporation is central to the PBH explosion baryogenesis mechanism discussed below.

The comoving PBH number density remains constant prior to complete evaporation. The corresponding Hawking energy released per unit comoving volume and unit time is therefore

$$\mathcal{E}^{\mathrm{co}}(\Delta t) \equiv n^{\mathrm{co}}_{\mathrm{PBH},\star} \left(-\frac{dM}{dt}\right) = n^{\mathrm{co}}_{\mathrm{PBH},\star} \frac{\mathcal{A}_f}{M^2(\Delta t)}. \tag{4.6}$$

This quantity describes the continuous transfer of PBH mass into relativistic Hawking radiation. Its contribution to the evolution of the radiation background and entropy is discussed in Sec. 4.2, while the directly emitted graviton component is treated separately in Sec. 6.1.

4.2 Radiation and entropy evolution

The Hawking evaporation of the PBH population transfers energy into the surrounding radiation bath and can modify both the expansion history and the entropy density of the Universe. Following Refs. [40, 68], we describe this evolution directly in terms of the physical PBH and radiation energy densities.

For the monochromatic PBH population considered here, the PBH energy density evolves according to

$$\dot{\rho}_{\mathrm{PBH}} + 3H\rho_{\mathrm{PBH}} = \frac{\dot{M}}{M}\rho_{\mathrm{PBH}}, \tag{4.7}$$

where the term $3H\rho_{\mathrm{PBH}}$ accounts for the dilution due to cosmic expansion, while the right-hand side describes the decrease of the PBH energy density associated with Hawking evaporation. Using Eq. (4.2), this equation becomes

$$\dot{\rho}_{\mathrm{PBH}} + 3H\rho_{\mathrm{PBH}} = -\frac{\mathcal{A}_f}{M^3(t)}\rho_{\mathrm{PBH}}. \tag{4.8}$$

The energy lost by the PBHs is injected into the surrounding radiation bath. The corresponding radiation energy density therefore satisfies [40, 68]

$$\dot{\rho}_{\mathrm{rad}} + 4H\rho_{\mathrm{rad}} = -\frac{\dot{M}}{M}\rho_{\mathrm{PBH}} = \frac{\mathcal{A}_f}{M^3(t)}\rho_{\mathrm{PBH}}. \tag{4.9}$$

The Hubble rate is determined self-consistently by the total energy density,

$$H^2 = \frac{1}{3M_{\mathrm{Pl}}^2}\left(\rho_{\mathrm{rad}} + \rho_{\mathrm{PBH}}\right), \qquad \frac{\dot{a}}{a} = H. \tag{4.10}$$

We take the horizon entry of the characteristic bubble scale as the starting point of the evaporation calculation. The scale factor at horizon entry is

$$a_{H,\star} = H_i \chi_i. \tag{4.11}$$

The physical PBH energy density at this epoch is therefore

$$\rho_{\rm PBH}|_{a=a_{H,\star}} = \frac{n^{\rm co}_{\rm PBH,\star} M_\star}{a^3_{H,\star}}. \tag{4.12}$$

The radiation energy density at horizon entry is

$$\rho_{\rm rad}|_{a=a_{H,\star}} \simeq 3 M_{\rm Pl}^2 H^2_{\rm form,\star}, \tag{4.13}$$

where the last approximation applies for $\kappa_H^{\rm SB} \ll 1$. The Universe is therefore radiation dominated at horizon entry. Since the PBH energy density redshifts more slowly than radiation, however, the PBH component can become dynamically important before evaporation.

Assuming that the Standard Model particles emitted by the PBHs thermalize efficiently with the ambient plasma, the background temperature is determined by

$$\rho_{\rm rad}(T_b) = \frac{\pi^2}{30} g_*(T_b) T_b^4, \tag{4.14}$$

and the entropy density is

$$s(T_b) = \frac{2\pi^2}{45} g_{*s}(T_b) T_b^3. \tag{4.15}$$

Following Ref. [47], for simplicity we approximate the effective relativistic degrees of freedom as constant throughout the numerical evolution relevant for baryogenesis and take

$$g_*(T_b) \simeq g_{*s}(T_b) \simeq 106.75. \tag{4.16}$$

For the entropy evolution, we use the comoving entropy density

$$s^{\rm co} \equiv a^3 s, \tag{4.17}$$

which evolves according to [47, 69]

$$\frac{ds^{\rm co}}{dt} = \frac{\mathcal{E}^{\rm co}}{T_b}. \tag{4.18}$$

Together with Eqs. (4.8), (4.9), and (4.10), these equations determine the radiation and entropy evolution throughout the PBH lifetime.

Whether the PBH population becomes dynamically dominant before evaporation depends on its initial abundance and lifetime. We discuss this condition in Sec. 6.2, where it determines the presence of the GW contribution sourced by PBH density fluctuations.

5 Electroweak Symmetry Restoration and Baryogenesis from Hawking Radiation of Light PBHs

We now estimate the baryon asymmetry that can be produced when the light PBHs originating from the spectator sector reach the final stage of Hawking evaporation. The microscopic thermalization, shock propagation, and CP-violating transport are described using the results of Refs. [47, 48]; we do not perform an independent hydrodynamic or electroweak transport simulation. Our calculation instead supplies the PBH population from the inflationary bubble source and follows its cosmological evolution. In particular, $M_\star$ and $n^{\rm co}_{{\rm PBH},\star}$ are determined by the nucleation and growth history, while $T_b(\Delta t)$ and $s^{\rm co}_{\rm max}$ are obtained from Sec. 4.2.

5.1 Landau–Pomeranchuk–Migdal thermalization and the explosive stage

During the final stage of PBH evaporation, the thermalization of the energetic QCD component of Hawking radiation is governed by the Landau–Pomeranchuk–Migdal (LPM) splitting rate in the surrounding plasma [47]. We evaluate the strong coupling using the one-loop QCD running [70–73],

$$\alpha_s(T_b) = \left[\alpha_s(m_Z)^{-1} + \frac{\beta_0}{2\pi}\ln\left(\frac{T_b}{m_Z}\right)\right]^{-1}, \qquad \beta_0 = 11 - \frac{2N_f}{3}. \tag{5.1}$$

For definiteness, we adopt $N_f = 6$ as a common benchmark throughout the temperature range considered. This choice is intended as a simplified estimate for the LPM thermalization calculation rather than a threshold-matched determination of the QCD running coupling. The corresponding LPM thermalization length is taken to be [47, 48]

$$L_{\rm LPM}(M, T_b) = \frac{1}{\alpha_s^2(T_b) T_b}\left[\frac{6\beta_{1/2} T_H(M)}{\pi C_R g_c T_b \ln\left[\beta_{1/2} T_H(M)/T_b\right]}\right]^{1/2}, \tag{5.2}$$

where

$$\beta_{1/2} = 4.53, \qquad C_R = C_F = \frac{4}{3}, \qquad g_c = 2N_c + N_f = 12, \qquad N_c = 3. \tag{5.3}$$

Here $\beta_{1/2} T_H$ characterizes the energy near the peak of the primary spin-1/2 Hawking spectrum, while $C_R = C_F$ corresponds to the quark-dominated color-charged component of the emission.

The final explosive stage begins when the remaining PBH lifetime becomes comparable to the thermalization scale of the emitted particles. In natural units, the threshold mass is therefore defined by [47, 48]

$$\tau[M_{\rm thres}(T_b)] = L_{\rm LPM}[M_{\rm thres}(T_b), T_b]\,, \tag{5.4}$$

which, using Eq. (4.4), becomes

$$\frac{M^3_{\rm thres}(T_b)}{3\mathcal{A}_f} = L_{\rm LPM}[M_{\rm thres}(T_b), T_b]\,. \tag{5.5}$$

For each background temperature T_b, Eq. (5.5) is solved numerically for the threshold mass $M_{\rm thres}$.

For the monochromatic population, all PBHs reach the threshold at the same time. With $\Delta t = 0$ defined at horizon entry as in Sec. 4.1, the explosion time is determined implicitly by

$$M_\star^3 - 3\mathcal{A}_f \Delta t_{\rm expl} = M_{\rm thres}^3[T_b(\Delta t_{\rm expl})]\,. \tag{5.6}$$

Since the initial PBH population is monochromatic, the comoving explosion rate is a single delta source,

$$\Gamma_{\rm expl}^{\rm co,SB}(\Delta t) = n_{\rm PBH,\star}^{\rm co}\,\delta(\Delta t - \Delta t_{\rm expl})\,. \tag{5.7}$$

5.2 Local electroweak symmetry restoration

When a PBH reaches $M_{\rm thres}$, its remaining energy is deposited over a region whose characteristic size is $L_{\rm LPM}$. Following the hydrodynamic treatment of Ref. [47], the effect of the preceding non-instantaneous heating stage is encoded by a factor K. We adopt the benchmark value $K = 5$ [48], which is representative of the hydrodynamic simulations used in Ref. [47]. The initial fireball temperature is then estimated from the ambient radiation energy density and the deposited energy as

$$T_{\rm fb}^4(T_b, K) = T_b^4 + \frac{90 K M_{\rm thres}(T_b)}{4\pi^3 g_{*,\rm EW} L_{\rm LPM}^3[M_{\rm thres}(T_b), T_b]}, \tag{5.8}$$

where $g_{*,\rm EW} = 106.75$. We use the electroweak restoration temperature $T_{\rm EW} = 162\,\mathrm{GeV}$, following Ref. [47, 48].

The minimum background temperature for which the explosion can still restore electroweak symmetry locally is defined by

$$T_{\rm fb}(T_{\rm min}, K) = T_{\rm EW}. \tag{5.9}$$

For $T_b < T_{\rm min}$, the final PBH explosion no longer heats the local plasma above $T_{\rm EW}$ and therefore does not contribute to the baryogenesis mechanism considered here.

The subsequent hydrodynamic evolution produces a finite region whose temperature exceeds the electroweak restoration scale. Following Refs. [47, 48], we characterize this region by its maximum radius $R_{\rm max}^{\rm EW}$, which determines the spatial volume relevant for the baryogenesis calculation below. The maximum radius reached by the electroweak-symmetric shell is parameterized by

$$R_{\rm max}^{\rm EW}(T_b) = 0.84 \left[\frac{K M_{\rm thres}(T_b)}{p(T_{\rm EW})}\right]^{1/3}, \tag{5.10}$$

with

$$p(T_{\rm EW}) = \frac{\pi^2}{90} g_{*,\rm EW} T_{\rm EW}^4. \tag{5.11}$$

The moving boundaries of this shell provide the out-of-equilibrium interfaces at which the local baryon asymmetry is generated.

5.3 Sphaleron window for baryogenesis

Baryogenesis is operative only when sphaleron processes in the ambient plasma are inefficient; otherwise the generated baryon asymmetry is washed out. We adopt the following parametrization for the sphaleron rate normalized by the temperature [47, 49, 50, 74],

$$\frac{\Gamma_{\rm spha}(T)}{T} = \begin{cases} 8.0 \times 10^{-7}, & T > T_{\rm EW}, \\ e^{-147.7+0.83(T/{\rm GeV})}, & T \leq T_{\rm EW}. \end{cases} \tag{5.12}$$

At a given time, the sphaleron freeze-out temperature is determined from the instantaneous expansion rate through

$$\Gamma_{\rm spha}[T_{\rm sph}(\Delta t)] = H(\Delta t). \tag{5.13}$$

The lower end of the baryogenesis temperature window is set by the loss of local electroweak restoration and is given by $T_{\rm min}$. For the monochromatic source, successful baryogenesis requires the background temperature at the explosion time to satisfy

$$T_{\rm min} < T_b(\Delta t_{\rm expl}) < T_{\rm sph}(\Delta t_{\rm expl}). \tag{5.14}$$

It is convenient to encode this condition by

$$\mathcal{I}_{\rm BG}(\Delta t) \equiv \Theta[T_b(\Delta t) - T_{\rm min}]\,\Theta[T_{\rm sph}(\Delta t) - T_b(\Delta t)]\,. \tag{5.15}$$

This form imposes the baryogenesis window directly in temperature space and does not require the background temperature to evolve monotonically.

The single explosion calculation also assumes that neighboring hydrodynamic shells do not overlap appreciably before the baryogenesis process is completed. Following the validity condition of Ref. [47], the characteristic physical PBH separation at the explosion time,

$$d_{\rm PBH}(\Delta t_{\rm expl}) = a(\Delta t_{\rm expl})\left(n^{\rm co}_{{\rm PBH},\star}\right)^{-1/3}, \tag{5.16}$$

is required to satisfy

$$d_{\rm PBH}(\Delta t_{\rm expl}) > R^{\rm EW}_{\rm max}[T_b(\Delta t_{\rm expl})]\,. \tag{5.17}$$

This condition ensures that the isolated-shock baryon yield used below remains a consistent approximation.

5.4 Baryon asymmetry

We now relate the baryon number generated by an individual PBH explosion to the resulting cosmological baryon asymmetry. In the baryogenesis sector, we adopt the effective dimension-five CP-violating interaction considered in Refs. [47, 75–77] and make use of the corresponding numerical results from their transport analysis,

$$\mathcal{L}_{\rm CPV} \supset -\frac{\mathcal{S}}{\Lambda}\,\overline{Q}_3\,\widetilde{H}\;(a_{\rm CPV} + i b_{\rm CPV}\gamma_5)\,t_R + {\rm h.c.}, \tag{5.18}$$

where $Q_3 = (t_L, b_L)^T$ denotes the third-generation left-handed quark doublet, t_R the right-handed top quark, $\widetilde{H} = i\sigma_2 H^*$, and $\mathcal{S}$ an additional scalar field associated with the CP-violating sector. The scale Λ characterizes the higher-dimensional interaction, while $b_{\rm CPV}$

controls its CP-violating component. We emphasize that $\mathcal{S}$ is introduced solely as part of the effective baryogenesis sector and is distinct from the spectator field s responsible for bubble nucleation in our construction.

For the benchmark wall profile and transport calculation considered in Ref. [47], the local baryon asymmetry generated at the moving interface can be parameterized as

$$\frac{\eta_B^{\rm loc}}{\eta_B^{\rm obs}} \simeq 10\, b_{\rm CPV} \left(\frac{1\,\text{TeV}}{\Lambda}\right)^2 , \tag{5.19}$$

where

$$\eta_B^{\rm obs} \equiv \frac{n_B}{s} = 8.65 \times 10^{-11}$$

denotes the observed baryon-to-entropy ratio [47, 75, 78–81]. It is convenient to define

$$C_{\rm CPV} \equiv \frac{\eta_B^{\rm loc}}{\eta_B^{\rm obs}} \left(\frac{\Lambda}{\text{TeV}}\right)^2 , \tag{5.20}$$

such that the benchmark adopted below corresponds to $C_{\rm CPV} \simeq 10\, b_{\rm CPV}$, with $b_{\rm CPV} = 1$.

For an individual PBH exploding in a plasma with background temperature T_b, we estimate the resulting baryon number by integrating over the region traversed by the electroweak-restoring interface [47],

$$N_B^{(1)}(T_b) = \eta_B^{\rm loc} s(T_{\rm EW}) \frac{4\pi}{3} \left[R_{\rm max}^{\rm EW}(T_b)\right]^3 . \tag{5.21}$$

Here, $\eta_B^{\rm loc} s(T_{\rm EW})$ gives the baryon number density generated locally as the electroweak-restoring interface propagates through the plasma, while the factor $4\pi[R_{\rm max}^{\rm EW}]^3/3$ represents the total volume swept out by the interface.

Approximating the plasma near the electroweak scale as a relativistic radiation fluid, one has

$$s(T_{\rm EW}) \simeq \frac{4p(T_{\rm EW})}{T_{\rm EW}} . \tag{5.22}$$

Together with Eqs. (5.10) and (5.11), this gives

$$N_B^{(1)}(T_b) = \eta_B^{\rm loc} (0.84)^3 \frac{16\pi}{3} \frac{K M_{\rm thres}(T_b)}{T_{\rm EW}} . \tag{5.23}$$

Using Eq. (5.20), the same result can be written as

$$N_B^{(1)}(T_b) = \eta_B^{\rm obs} C_{\rm CPV} \left(\frac{\text{TeV}}{\Lambda}\right)^2 (0.84)^3 \frac{16\pi}{3} \frac{K M_{\rm thres}(T_b)}{T_{\rm EW}} . \tag{5.24}$$

The cumulative baryon number per unit comoving volume is then

$$n_B^{\rm co} = \int d\Delta t\, N_B^{(1)}[T_b(\Delta t)] \Gamma_{\rm expl}^{\rm co,SB}(\Delta t) \mathcal{I}_{\rm BG}(\Delta t), \tag{5.25}$$

where $\Gamma_{\rm expl}^{\rm co,SB}$ is the explosion rate per unit comoving volume and $\mathcal{I}_{\rm BG}$ implements the conditions under which shock baryogenesis is operative.

For the monochromatic source in Eq. (5.7), all PBHs undergo their final explosive stage at the same time, and Eq. (5.25) reduces to

$$n_B^{\rm co} = n_{\rm PBH,\star}^{\rm co} N_B^{(1)}[T_b(\Delta t_{\rm expl})]\,\mathcal{I}_{\rm BG}(\Delta t_{\rm expl}). \tag{5.26}$$

The total comoving baryon number is therefore directly proportional to the comoving PBH abundance inherited from the bubble nucleation history. The final baryon-to-entropy ratio, however, also depends on the entropy generated during PBH evaporation, as discussed below.

To compare the generated asymmetry with the observed value, we define

$$Y_{\rm SB} \equiv \frac{\eta_{B,\rm SB}^{\rm tot}}{\eta_B^{\rm obs}}, \qquad Y_{\rm scaled}^{\rm SB} \equiv Y_{\rm SB}\left(\frac{\Lambda}{\rm TeV}\right)^2. \tag{5.27}$$

The thermal evolution discussed in Sec. 4.2 determines the comoving entropy density $s^{\rm co} = a^3 s$. During PBH evaporation, entropy injection causes $s^{\rm co}$ to increase, while after complete evaporation it approaches the asymptotic value $s_{\rm max}^{\rm co}$ and remains conserved thereafter. Since $n_B^{\rm co}$ and $s_{\rm max}^{\rm co}$ are defined using the same comoving-volume normalization, the final baryon-to-entropy ratio is simply

$$\eta_{B,\rm SB}^{\rm tot} = \frac{n_B^{\rm co}}{s_{\rm max}^{\rm co}}. \tag{5.28}$$

Here, $s_{\rm max}^{\rm co}$ is the asymptotic comoving entropy density reached after the entropy injection from PBH evaporation has ended.

Combining Eqs. (5.24), (5.25), (5.27), and (5.28), the scaled cosmological yield becomes

$$Y_{\rm scaled}^{\rm SB} = \mathcal{Q}_{\rm phys}^{\rm SB} \int d\Delta t\, M_{\rm thres}[T_b(\Delta t)]\Gamma_{\rm expl}^{\rm co,SB}(\Delta t)\mathcal{I}_{\rm BG}(\Delta t), \tag{5.29}$$

with

$$\mathcal{Q}_{\rm phys}^{\rm SB} = C_{\rm CPV}(0.84)^3 \frac{16\pi}{3}\frac{K}{T_{\rm EW}}\frac{1}{s_{\rm max}^{\rm co}}. \tag{5.30}$$

Thus, all entropy dilution associated with the PBH evaporation history is encoded directly in the asymptotic comoving entropy density $s_{\rm max}^{\rm co}$.

Finally, substituting the monochromatic explosion rate gives

$$\begin{aligned} Y_{\rm scaled}^{\rm SB} = {} & \mathcal{Q}_{\rm phys}^{\rm SB} n_{\rm PBH,\star}^{\rm co} M_{\rm thres}[T_b(\Delta t_{\rm expl})] \\ & \times \Theta[T_b(\Delta t_{\rm expl}) - T_{\rm min}]\,\Theta[T_{\rm sph}(\Delta t_{\rm expl}) - T_b(\Delta t_{\rm expl})]\,. \end{aligned} \tag{5.31}$$

The final baryon asymmetry is therefore controlled by both the comoving PBH abundance and the entropy generated during PBH evaporation, together with the thermal and hydrodynamic conditions governing the final explosive stage. In particular, once the PBH abundance is sufficiently large for a PBH dominated epoch to develop, increasing the PBH population also increases the entropy injected during evaporation. As found in Ref. [47], these two effects can approximately compensate each other, causing the final baryon yield to approach a saturation value rather than continuing to grow linearly with the PBH abundance.

6 GW Signatures

The PBH population generated by the spectator sector transition gives rise to two qualitatively distinct GW contributions. First, gravitons are emitted directly through Hawking radiation from the PBHs. This contribution is present regardless of whether the PBHs ever dominate the cosmic energy density. Second, if the PBH abundance is sufficiently large to produce a transient PBH dominated epoch before evaporation, fluctuations in the PBH number density source scalar perturbations that subsequently induce GWs at second order. These two production mechanisms are illustrated schematically in Fig. 1(e) and (c), respectively, and are discussed separately below [51–54].

6.1 GWs from Hawking radiation

For the nonrotating PBHs considered here, the instantaneous graviton energy spectrum can be written as [51, 67]

$$\frac{d^2E_g}{dt\,d\omega} = \frac{1}{2\pi}\sum_{\ell,m}\frac{\omega\,\Gamma^{(2)}_{\ell m}(\omega, M)}{e^{\omega/T_H(M)}-1}, \tag{6.1}$$

where $\Gamma^{(2)}_{\ell m}$ denotes the spin-2 greybody factor, including the graviton polarization multiplicity, and $T_H(M) = M_{\rm Pl}^2/M$ is the Hawking temperature in the reduced Planck mass convention adopted throughout this work. The greybody factor encodes the propagation of the emitted gravitons through the Schwarzschild geometry and therefore modifies the emission spectrum relative to that of an ideal blackbody [51].

As the PBH evaporates, its mass decreases according to Eq. (4.3), while its Hawking temperature increases. The graviton spectrum observed today therefore receives contributions from the entire evaporation history, with the emitted frequencies subsequently redshifted by the cosmological expansion. A complete calculation can be performed by integrating Eq. (6.1) over the evolving PBH mass and background history, as discussed in Ref. [51].

For the numerical evaluation of the Hawking contribution, we recast the semi-analytic estimate of Ref. [55] in terms of the PBH parameters obtained in our scenario. It is convenient to separate the overall normalization from the frequency dependence and write

$$\Omega^{\rm Haw}_{\rm GW,0}(f_0)h^2 = \mathcal{A}_{\rm Haw}\left(\frac{f_0}{10^9\,\rm Hz}\right)^4 \mathcal{F}_{\rm Haw}\left(x_0; z^{\rm SB}_{\rm max}\right), \tag{6.2}$$

where

$$\mathcal{A}_{\rm Haw} = 1.36\times10^{-21}\left(\frac{g_{*,H,\star}}{100}\right)^2\left(\frac{1\,\rm g}{M_\star}\right)^2, \tag{6.3}$$

and

$$x_0 \equiv \frac{2\pi f_0}{T^{\rm SB}_{\rm BH,0}}. \tag{6.4}$$

Here $g_{*,H,\star} \equiv g_{*,H}[T_H(M_\star)]$ denotes the effective number of particle degrees of freedom contributing to Hawking evaporation at the initial PBH temperature.

The quantity $T^{\rm SB}_{\rm BH,0}$ characterizes the Hawking temperature redshifted to the present epoch and expressed in frequency units. For the monochromatic PBH population considered here, it is approximated by

$$T^{\rm SB}_{\rm BH,0} \simeq 4.53\times10^{15}\,{\rm Hz}\left(\frac{M_\star}{10^5\,{\rm g}}\right)^{1/2}\left[\frac{100}{g_{*s}(T_{\rm ev})}\right]^{1/12}\left(\frac{100}{g_{*,H,\star}}\right)^{1/2}, \tag{6.5}$$

where $T_{\rm ev}$ is the background temperature at the completion of PBH evaporation. The factor 2π in Eq. (6.4) accounts for the conversion between the ordinary frequency f_0 and the corresponding angular frequency.

The spectral shape is encoded in

$$\mathcal{F}_{\rm Haw}\left(x_0; z^{\rm SB}_{\rm max}\right) = \int_1^{1+z^{\rm SB}_{\rm max}} dy\,\frac{y^{1/2}}{e^{x_0 y}-1}, \tag{6.6}$$

where we have introduced $y = 1+z$. The upper integration limit is determined by

$$1+z^{\rm SB}_{\rm max} \simeq 7.36\times10^{7}\left(\frac{M_\star}{1\,{\rm g}}\right)^{4/3}\left(\kappa^{\rm SB}_H\right)^{1/3}. \tag{6.7}$$

Here $\kappa^{\rm SB}_H$ denotes the PBH abundance at horizon entry, as defined in Eq. (3.23). Since the PBH energy density at formation is much smaller than the radiation energy density in the parameter region considered here, the PBH-to-radiation ratio $\rho_{\rm PBH}/\rho_{\rm rad}$ and the PBH fraction of the total energy density $\rho_{\rm PBH}/\rho_{\rm tot}$ are numerically equivalent to the accuracy relevant for this work. We therefore do not distinguish between the two conventions and denote both by $\kappa^{\rm SB}_H$. Both $M_\star$ and $\kappa^{\rm SB}_H$ are determined by the spectator sector tunneling history and are therefore not independent inputs.

The direct Hawking-graviton signal is a generic consequence of PBH evaporation. The semi-analytic spectrum above is adopted for the benchmark cosmological history in which the PBH population undergoes an early PBH dominated epoch before evaporation [55]. The condition for realizing this epoch is discussed in Sec. 6.2.

6.2 GWs induced by PBH density fluctuations

The GW contribution induced by PBH density fluctuations is relevant only if the PBH population becomes dynamically dominant before evaporation. We therefore first specify the corresponding abundance and consistency conditions associated with big bang nucleosynthesis (BBN) before discussing the GW spectrum.

In the PBH dominated branch, the temperature of the radiation bath after evaporation can be estimated as [53]

$$T_{\rm ev} \simeq 2.70\times10^{4}\,{\rm GeV}\left(\frac{M_\star}{10^4\,{\rm g}}\right)^{-3/2}\left[\frac{g_{*,H,\star}}{100}\right]^{1/2}\left[\frac{g_*(T_{\rm ev})}{100}\right]^{-1/4}, \tag{6.8}$$

where $g_{*,H,\star} \equiv g_{*,H}[T_H(M_\star)]$ denotes the effective number of particle degrees of freedom contributing to Hawking evaporation at the initial PBH temperature. Requiring the PBHs to evaporate sufficiently early for successful BBN, we impose the conservative condition $T_{\rm ev} > 4\,{\rm MeV}$, which gives the approximate upper bound $M_\star \lesssim 4\times10^{8}\,{\rm g}$.

For the PBH dominated branch considered here, the PBHs must become the dominant component before evaporation. During radiation domination, the PBH energy density redshifts as a^{-3}, whereas the radiation energy density redshifts as a^{-4}, so that the PBH fraction grows with the scale factor. Requiring PBH domination to occur before evaporation therefore imposes a lower bound on the initial PBH abundance [53]. With the horizon-mass convention adopted in this work, we use

$$\kappa_H^{\rm SB} \gtrsim \kappa_{\rm min}^{\rm SB}, \qquad \kappa_{\rm min}^{\rm SB} \simeq 2.84\times10^{-10}\left(\frac{M_\star}{10^4\,\mathrm{g}}\right)^{-1}\left[\frac{g_{*,H,\star}}{100}\right]^{1/2}. \tag{6.9}$$

For a monochromatic and initially unclustered PBH population that undergoes an early PBH dominated epoch, Poisson density fluctuations generate an additional GW background. The requirement that this induced GW contribution remain consistent with BBN places an upper bound on the initial PBH abundance [53]. In the mass convention adopted here, this bound is

$$\kappa_H^{\rm SB} \lesssim \kappa_{\rm max}^{\rm GW/BBN}, \tag{6.10}$$

with

$$\kappa_{\rm max}^{\rm GW/BBN} \simeq 4.92\times10^{-7}\left(\frac{M_\star}{10^4\,\mathrm{g}}\right)^{-17/24}\left[\frac{g_{*,H,\star}}{100}\right]^{17/48}\left[\frac{g_*(T_{\rm ev})}{100}\right]^{1/16}. \tag{6.11}$$

This constraint assumes a narrow PBH mass distribution, approximately Poisson spatial statistics, a PBH dominated epoch before evaporation, and the sudden-evaporation treatment used in Ref. [53].

The parameter region relevant for the density fluctuation GW signal therefore satisfies

$$\kappa_{\rm min}^{\rm SB} \lesssim \kappa_H^{\rm SB} \lesssim \kappa_{\rm max}^{\rm GW/BBN}, \tag{6.12}$$

together with the pre-BBN evaporation condition. For the benchmark values $g_{*,H,\star} \simeq 100$ and $g_*(T_{\rm ev}) \simeq 100$, the corresponding abundance interval becomes

$$2.84\times10^{-10}\left(\frac{M_\star}{10^4\,\mathrm{g}}\right)^{-1} \lesssim \kappa_H^{\rm SB} \lesssim 4.92\times10^{-7}\left(\frac{M_\star}{10^4\,\mathrm{g}}\right)^{-17/24}. \tag{6.13}$$

We now turn to the associated GW spectrum. Even in the absence of primordial clustering, the discrete nature of the PBH population generates Poisson fluctuations in its number density. These fluctuations initially correspond to isocurvature perturbations. During a PBH dominated epoch, they source scalar metric perturbations, which subsequently generate GWs at second order. The production is strongly enhanced around the transition from PBH domination back to radiation domination at evaporation [53].

Following the semi-analytic template used in Ref. [55], we approximate the present-day spectrum as

$$\Omega_{\rm GW,0}^{\rm DF}(f)h^2 \simeq \Omega_{\rm GW,0}^{\rm DF,peak}h^2\left(\frac{f}{f_{\rm peak}^{\rm DF}}\right)^{11/3}\Theta\big(f_{\rm peak}^{\rm DF}-f\big)\,. \tag{6.14}$$

The spectrum therefore rises approximately as $f^{11/3}$ below the peak and is cut off at the ultraviolet scale associated with the mean PBH separation [53, 55].

Expressed directly in terms of the PBH-to-radiation ratio derived in our scenario, the peak amplitude is

$$\Omega_{\mathrm{GW},0}^{\mathrm{DF,peak}} \simeq 1.46 \times 10^{-4} \left(\frac{M_\star}{10^7\,\mathrm{g}}\right)^{34/9} \left(\frac{\kappa_H^{\mathrm{SB}}}{10^{-8}}\right)^{16/3}. \tag{6.15}$$

The corresponding peak frequency is

$$f_{\mathrm{peak}}^{\mathrm{DF}} \simeq 1.7 \times 10^3\,\mathrm{Hz} \left(\frac{M_\star}{10^4\,\mathrm{g}}\right)^{-5/6}. \tag{6.16}$$

Thus lighter PBHs shift the signal toward higher frequencies, whereas the peak amplitude depends strongly on both the PBH mass and the abundance inherited from the spectator sector tunneling history.

The template in Eqs. (6.14)–(6.16) is applied only to parameter points that undergo an early PBH dominated epoch. It further assumes a sufficiently narrow PBH mass distribution and an approximately Poisson spatial distribution.

7 Numerical Results

We now present the numerical results of the spectator sector scenario developed in the preceding sections. Throughout this section, we fix

$$\Delta N_{\mathrm{nuc}} = 1 \tag{7.1}$$

as a common benchmark. As can be seen from Eq. (2.27), the bubble number density depends linearly on the duration of the nucleation interval, whereas its dominant sensitivity arises from the nucleation rate $\Gamma_\star$, which depends exponentially on the tunneling action. The abundance can therefore vary substantially through changes in the spectator potential parameters, making $\Delta N_{\mathrm{nuc}} = 1$ a representative choice for the numerical analysis. We further consider two benchmark values of the effective wall velocity,

$$v_{\mathrm{eff}} = 0.3, \qquad v_{\mathrm{eff}} = 0.7. \tag{7.2}$$

As discussed in Sec. 3.1, v_{eff} is treated as a phenomenological parameter characterizing the accumulated wall propagation during inflation. A first-principles determination of this quantity would require solving the time-dependent bubble wall dynamics in the evolving spectator potential. The benchmark values above are therefore used to explore the resulting PBH phenomenology within the effective description adopted in this work.

For each value of v_{eff}, we scan the remaining model parameters and retain only points satisfying the vacuum structure, tunneling, stability of the bubble interior, supercriticality, PBH formation, and cosmological consistency conditions discussed in the preceding sections. In addition, we restrict the numerical scan to the PBH dominated branch, requiring the PBH abundance to be sufficiently large for the PBHs to dominate the cosmic energy density before evaporation. This restriction ensures a sufficiently large PBH population

and selects the regime in which the density fluctuation GW signal can be significantly enhanced.

The resulting PBH population gives rise to two distinct GW contributions: direct Hawking emission of gravitons and GWs induced by PBH density fluctuations. Their prospects for detection depend on both the signal amplitude and the frequency range in which the spectrum is peaked. In the parameter region considered here, the density fluctuation contribution lies in a frequency range more favorable for potential detection, whereas the Hawking graviton contribution peaks at much higher frequencies. We therefore select the GW benchmark points according to the peak amplitude of the density fluctuation contribution,

$$\Omega_{\mathrm{GW},0}^{\mathrm{DF,peak}} h^2 \equiv \max_f \left[\Omega_{\mathrm{GW},0}^{\mathrm{DF}}(f) h^2\right]. \tag{7.3}$$

For each value of v_{eff}, the five viable points with the largest $\Omega_{\mathrm{GW},0}^{\mathrm{DF,peak}} h^2$ are retained as benchmark points. This selection is intended to highlight the region of the viable parameter space with the most favorable density fluctuation GW signals and should not be interpreted as representative of the full viable parameter region.

The properties of the selected benchmark points are summarized in Table 1. The first five points correspond to $v_{\mathrm{eff}} = 0.3$, while the remaining five correspond to $v_{\mathrm{eff}} = 0.7$. Within each group, the points are ordered according to decreasing $\Omega_{\mathrm{GW},0}^{\mathrm{DF,peak}} h^2$.

To assess the validity of the monochromatic-limit treatment for these benchmarks, we further reconstruct the nucleation history across the corresponding inflationary interval. We use the number-weighted comoving PBH source,

$$\mathcal{P}_N(N) \propto \frac{e^{-3N}\Gamma(N)}{H(N)}, \qquad \int dN\, \mathcal{P}_N(N) = 1, \tag{7.4}$$

and define ΔN_{90} as the narrowest continuous interval in N containing 90% of the resulting PBH number abundance.

As a conservative test, we evaluate this quantity using the largest allowed potential-profile width $\sigma_{N,\max}$ for each benchmark point. Although these widths can be of order unity and can become moderately broad for some benchmark points, the corresponding PBH-producing nucleation histories remain substantially more localized because of the exponential dependence of the tunneling rate on the bounce action. For all ten benchmark points we find

$$\Delta N_{90} < 1. \tag{7.5}$$

Moreover, the intervals containing 95% of the PBH number abundance are also narrower than one e-fold for all benchmark points. These results demonstrate that the PBH-producing nucleation history can be substantially more localized than the underlying spectator potential feature, even when the latter extends over a relatively broad interval. This localization provides support for the monochromatic approximation adopted in Sec. 3.4, while confirming that the physical nucleation width relevant for the PBH mass distribution is not determined directly by σ_N.

The selected points span characteristic PBH masses from $3.985 \times 10^5\,\mathrm{g}$ to $4.024 \times 10^6\,\mathrm{g}$. These masses follow from the bubble scale acquired during inflation and are not

Table 1: Benchmark points for $\Delta N_{\rm nuc} = 1$ and $v_{\rm eff} = 0.3$ or 0.7. For each value of $v_{\rm eff}$, the five viable points with the largest peak amplitude of the GW signal induced by PBH density fluctuations are shown. The PBH mass, abundance, baryon yield, and GW observables are derived quantities, while the corresponding spectator potential parameters are listed in Table 2. The baryon yield is evaluated for the benchmark $\Lambda = 1$ TeV.

BP	$v_{\rm eff}$	$N_\star$	$M_\star$ [g]	$\kappa_H^{\rm SB}$	$Y_{\rm SB}$	$f_{\rm peak}^{\rm DF}$ [Hz]	$\Omega_{\rm GW,0}^{\rm DF,peak}h^2$
BP1	0.3	7.5172	4.024×10^6	6.567×10^{-9}	1.141×10^{-3}	1.148×10^1	2.26×10^{-7}
BP2	0.3	6.2759	3.096×10^6	6.541×10^{-9}	1.956×10^{-3}	1.428×10^1	8.215×10^{-8}
BP3	0.3	7.2069	2.162×10^6	6.563×10^{-9}	4.064×10^{-3}	1.926×10^1	2.157×10^{-8}
BP4	0.3	5.0345	2.366×10^6	6.088×10^{-9}	3.385×10^{-3}	1.787×10^1	2.028×10^{-8}
BP5	0.3	5.9655	1.662×10^6	6.527×10^{-9}	6.919×10^{-3}	2.399×10^1	7.748×10^{-9}
BP6	0.7	4.4138	3.985×10^5	3.203×10^{-8}	1.192×10^{-1}	7.885×10^1	1.701×10^{-7}
BP7	0.7	5.9655	9.796×10^5	1.238×10^{-8}	1.998×10^{-2}	3.726×10^1	3.197×10^{-8}
BP8	0.7	5.6552	5.256×10^5	1.235×10^{-8}	6.891×10^{-2}	6.26×10^1	2.998×10^{-9}
BP9	0.7	6.5862	3.398×10^6	1.713×10^{-11}	1.57×10^{-3}	1.322×10^1	1.984×10^{-21}
BP10	0.7	4.4138	3.681×10^6	1.54×10^{-11}	1.331×10^{-3}	1.236×10^1	1.522×10^{-21}

independently adjusted to obtain the GW signal. Within the approximation adopted in Sec. 3.3, the characteristic mass scales as

$$M_\star \simeq \frac{v_{\rm eff}^2}{2GH_i}\left(e^{N_\star} - 1\right)^2 . \tag{7.6}$$

Changing $v_{\rm eff}$ therefore modifies the mapping between the inflationary nucleation history and the PBH mass scale. Since the remaining model parameters are varied simultaneously, however, the two samples should not be related by a simple rescaling with $v_{\rm eff}$.

For all benchmark points, the PBH-to-radiation ratio at horizon entry remains small,

$$\kappa_H^{\rm SB} \ll 1, \tag{7.7}$$

with the values in Table 1 ranging from approximately 1.6×10^{-11} to 3.2×10^{-8}. The Universe is therefore radiation dominated when the PBHs form. The points for which the density fluctuation GW contribution is evaluated subsequently satisfy the condition for an intermediate PBH dominated epoch before evaporation, together with the pre-BBN evaporation requirement discussed in Sec. 6.2.

The same PBH population can generate a baryon asymmetry through the explosive stage of Hawking evaporation. For the benchmark CP-violating scale $\Lambda = 1$ TeV, the normalized baryon yield can reach

$$Y_{\rm SB} \sim \mathcal{O}(10^{-1}) \tag{7.8}$$

within the viable parameter region. The benchmark points displayed in Table 1 are selected according to their density fluctuation GW signals rather than their baryon yield and therefore do not necessarily include the points that maximize $Y_{\rm SB}$. Nevertheless, the

displayed benchmarks already show that a sizable baryon asymmetry can be generated in the same region of parameter space that gives interesting GW signals. In particular, BP6 gives

$$Y_{\rm SB}^{\rm BP6} = 1.192 \times 10^{-1}, \tag{7.9}$$

corresponding to about 12% of the observed baryon asymmetry for the benchmark interaction adopted here.

As emphasized in Sec. 5.4, these values should be regarded as order-of-magnitude estimates of the baryogenesis potential of the scenario. With the normalization adopted there, the baryon yield scales as

$$Y_{\rm SB} \propto \left(\frac{\rm TeV}{\Lambda}\right)^2 . \tag{7.10}$$

The numerical results quoted here therefore refer specifically to the benchmark $\Lambda = 1$ TeV and should not be interpreted as a model-independent upper limit on the baryon asymmetry.

The upper range of $Y_{\rm SB}$ found in the present scan is primarily associated with entropy production during PBH evaporation. The saturation behavior can be understood directly from the ratio $n_B^{\rm co}/s_{\rm max}^{\rm co}$. In the PBH dominated regime, increasing the initial PBH abundance enhances both the integrated baryon production and the entropy generated by evaporation. Their common dependence on the PBH population therefore weakens the sensitivity of the final baryon-to-entropy ratio to a further increase in the initial abundance, consistent with the behavior found in Ref. [47].

The value of the saturation level is specific to the baryogenesis realization and benchmark parameters adopted here. In particular, it depends on the CP-violating interaction, the hydrodynamic properties of the explosion, and the thermal history entering $M_{\rm thres}$ and the baryogenesis window. Other choices of the CP-violating interaction, or alternative baryogenesis mechanisms with a larger baryon yield per PBH, could therefore modify the saturation value without requiring a correspondingly larger PBH abundance.

We now turn to the GW spectra of the benchmark points listed in Table 1. Figure 2 shows the present-day spectra for $v_{\rm eff} = 0.3$ in the left panel and $v_{\rm eff} = 0.7$ in the right panel. For each value of $v_{\rm eff}$, the five displayed spectra correspond to the viable points with the largest peak amplitudes of the GW contribution induced by PBH density fluctuations.

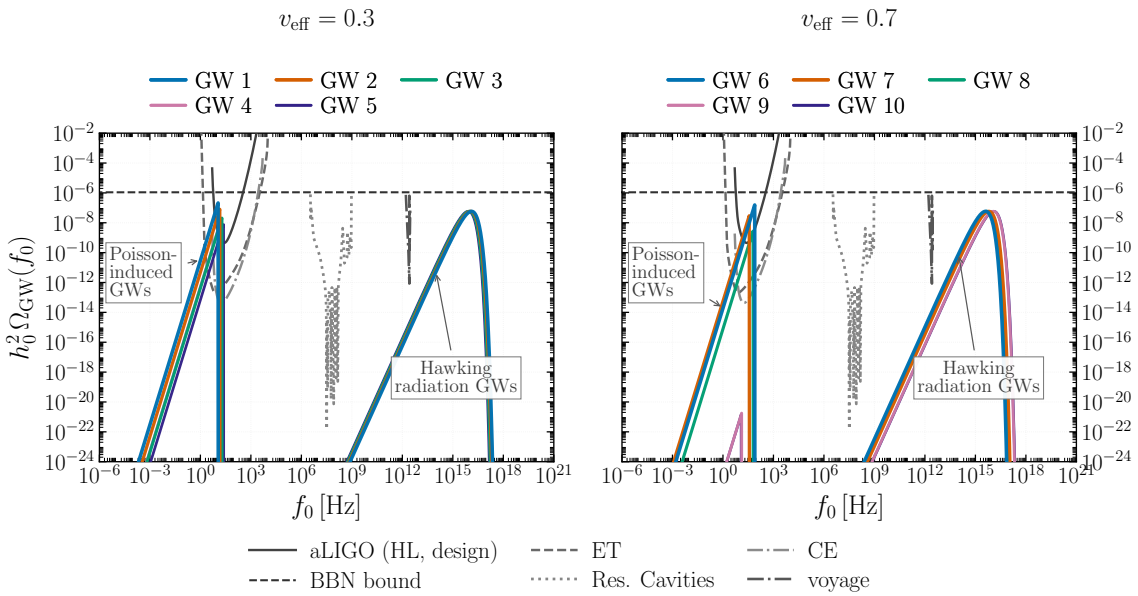


Figure 2: Present-day GW spectra for the benchmark points listed in Table 1. The left and right panels correspond to $v_{\rm eff} = 0.3$ and $v_{\rm eff} = 0.7$, respectively, with $\Delta N_{\rm nuc} = 1$ in both cases. For each value of $v_{\rm eff}$, the five points are selected according to the peak amplitude $\Omega_{\rm GW,0}^{\rm DF,peak}h^2$ of the GW contribution induced by PBH density fluctuations. The lower frequency feature is generated by PBH density fluctuations during the PBH dominated epoch, whereas the high frequency feature originates from direct Hawking emission of gravitons. Reference power-law-integrated sensitivity curves (PLISCs) [82] for the Advanced LIGO Hanford–Livingston (HL) detector network at design sensitivity [83], the Einstein Telescope (ET) [84], and Cosmic Explorer (CE) [85] are shown together with representative high-frequency sensitivities from resonant electromagnetic detectors [86] and searches based on the inverse Gertsenshtein effect [87]. The BBN reference bound is also indicated [88, 89].

The two well-separated features in Fig. 2 arise from different production mechanisms. The lower frequency contribution is induced by PBH density fluctuations during the intermediate PBH dominated epoch, whereas the high frequency contribution originates from gravitons emitted directly through Hawking evaporation. Their widely separated characteristic frequencies therefore reflect the distinct physical scales involved in these two mechanisms.

For $v_{\rm eff} = 0.3$, the density fluctuation signals are concentrated within a relatively narrow frequency interval,

$$11.48\ \text{Hz} \lesssim f_{\rm peak}^{\rm DF} \lesssim 23.99\ \text{Hz}, \tag{7.11}$$

with peak amplitudes in the range

$$7.75 \times 10^{-9} \lesssim \Omega_{\rm GW,0}^{\rm DF,peak}h^2 \lesssim 2.26 \times 10^{-7}. \tag{7.12}$$

The upper end of this range is realized by BP1,

$$f_{\rm peak}^{\rm DF} = 11.48 \text{ Hz}, \qquad \Omega_{\rm GW,0}^{\rm DF,peak} h^2 = 2.26 \times 10^{-7}, \tag{7.13}$$

while the remaining benchmarks exhibit a gradual reduction in the peak amplitude. The corresponding frequencies remain in the tens-of-hertz range relevant for ground-based interferometric searches.

A qualitatively broader distribution is obtained for $v_{\rm eff} = 0.7$. In this case, the peak frequencies extend over

$$12.36 \text{ Hz} \lesssim f_{\rm peak}^{\rm DF} \lesssim 78.85 \text{ Hz}, \tag{7.14}$$

and the peak amplitudes span several orders of magnitude. The largest signal is obtained for BP6,

$$f_{\rm peak}^{\rm DF} = 78.85 \text{ Hz}, \qquad \Omega_{\rm GW,0}^{\rm DF,peak} h^2 = 1.70 \times 10^{-7}. \tag{7.15}$$

While BP7 and BP8 still yield peak amplitudes of order 10^{-8} and 10^{-9}, respectively, the signals from BP9 and BP10 are strongly suppressed, reaching only order 10^{-21}. Thus, increasing $v_{\rm eff}$ does not simply shift the characteristic frequency, but is accompanied by a much wider variation in the density fluctuation GW amplitude across the viable benchmark points.

This large variation follows from the strong dependence of the density fluctuation contribution on the PBH abundance. From Eq. (6.15),

$$\Omega_{\rm GW,0}^{\rm DF,peak} \propto \left(\kappa_H^{\rm SB}\right)^{16/3} M_\star^{34/9}. \tag{7.16}$$

Although BP9 and BP10 have comparatively large PBH masses, their abundances are only of order 10^{-11}, and the steep dependence on $\kappa_H^{\rm SB}$ suppresses their density fluctuation signals by many orders of magnitude. In contrast, BP1 and BP6 have substantially larger PBH abundances and consequently produce the largest signals in the two benchmark samples. The peak frequency is controlled mainly by the PBH mass through

$$f_{\rm peak}^{\rm DF} \propto M_\star^{-5/6}, \tag{7.17}$$

so that lighter PBHs generally shift the density fluctuation signal toward higher frequencies.

The leading density fluctuation signals therefore lie mainly in the $\mathcal{O}(10)$–$\mathcal{O}(10^2)$ Hz range and can reach

$$\Omega_{\rm GW,0}^{\rm DF,peak} h^2 \sim \mathcal{O}(10^{-7}). \tag{7.18}$$

As illustrated in Fig. 2, this places the strongest benchmarks in a frequency and amplitude region relevant for ground-based GW experiments. The sensitivity curves shown in the figure are used to indicate the experimentally relevant region [82].

The Hawking-graviton contribution occupies a qualitatively different frequency range. For the benchmark masses considered here, the broad Hawking feature peaks at frequencies of order 10^{16} Hz. The amplitudes of the corresponding spectra vary much less dramatically than those of the density fluctuation contribution because the latter depends very strongly on the PBH abundance. The principal challenge for the Hawking signal is instead its

extremely high characteristic frequency. Resonant electromagnetic detectors and searches based on graviton-photon conversion have been proposed as possible probes of high frequency GWs [86, 87]. The Hawking peaks displayed in Fig. 2, however, remain outside the reference sensitivity regions shown in the figure. We therefore use the density fluctuation contribution, rather than the Hawking component, to rank the benchmark points.

The comparison between the two panels also shows that changing $v_{\rm eff}$ does not produce a simple uniform shift of the GW spectra. The effective wall velocity changes the bubble scale acquired during inflation and hence the PBH mass associated with a given nucleation history, while the spectator sector parameters simultaneously determine the tunneling rate and the PBH abundance. Consequently, both the peak frequency and the peak amplitude are controlled by the correlated values of $M_\star$ and $\kappa_H^{\rm SB}$ rather than by $v_{\rm eff}$ alone.

Overall, the numerical results exhibit a characteristic two-scale GW signature produced by the same PBH population: a very high frequency component from direct Hawking graviton emission and a much lower frequency component induced by PBH density fluctuations. In the parameter region considered here, the latter extends into the frequency range relevant for ground-based interferometers and provides the more promising observational probe of the scenario.

8 Conclusions

In this work, we have investigated the formation of light PBHs from vacuum bubbles nucleated during a spectator sector FOPT in inflation, together with their subsequent cosmological consequences. A central feature of our scenario is that the spectator potential evolves with the rolling inflaton, allowing vacuum bubbles to nucleate and grow during inflation before the vacuum ordering reverses near its end. The resulting bubbles contain metastable false vacuum interiors, whose stability against reverse vacuum tunneling is essential for their subsequent evolution. We account for this requirement by imposing benchmark stability conditions before and after reheating. Sufficiently large bubbles can then undergo supercritical evolution and form PBHs in the parent universe [29]. Within this framework, the PBH abundance is determined by the integrated vacuum tunneling history, while the characteristic mass depends on the nucleation epoch and the accumulated bubble growth during inflation. Our numerical results further indicate that the PBH-producing nucleation history can remain sharply localized even when the spectator potential evolves over a broader interval, supporting the monochromatic approximation adopted in our benchmark analysis.

We have further followed the subsequent Hawking evolution of the resulting PBH population and its impact on the cosmological radiation and entropy background. When the remaining PBH lifetime becomes comparable to the LPM thermalization scale, the final stage of evaporation can lead to an explosive release of energy into the surrounding plasma. Following the mechanism of Ref. [47], this energy deposition can restore electroweak symmetry locally even after sphaleron processes in the ambient Universe have frozen out. The resulting finite interval between ambient sphaleron freeze-out and the loss of local electroweak restoration defines the baryogenesis window in our scenario.

For the benchmark choice $\Lambda = 1$ TeV adopted in Ref. [47], we find that the normalized baryon yield can reach

$$Y_{\rm SB} \equiv \frac{\eta_{B,\rm SB}^{\rm tot}}{\eta_B^{\rm obs}} \sim \mathcal{O}(10^{-1}) \tag{8.1}$$

for the most favorable parameter points considered in our analysis. Thus, for the benchmark interaction adopted here, exploding PBHs produced by the spectator sector phase transition can generate a baryon asymmetry at the ten-percent level relative to the observed value. At sufficiently large PBH abundance, the enhancement of the baryon number from the larger number of PBH explosions is accompanied by increased entropy production during evaporation, causing the final baryon yield to approach a saturation value, as also found in Ref. [47]. Since the CP-violating source adopted here scales as $(\mathrm{TeV}/\Lambda)^2$, the numerical saturation level should be understood as a benchmark-dependent result rather than as a model-independent upper limit.

More importantly, the present calculation should be regarded as an order-of-magnitude estimate of the baryogenesis potential of this mechanism. Several ingredients, including the bubble wall evolution, the mapping from the bubble scale acquired during inflation to the PBH mass, the hydrodynamic evolution of the final explosion, and the effective CP-violating interaction, have been treated phenomenologically. Nevertheless, the fact that the resulting baryon asymmetry can reach a sizable fraction of the observed value suggests that a spectator sector phase transition followed by PBH formation and evaporation may provide a phenomenologically relevant source of baryon number.

The required new physics enters at several stages of the mechanism. In addition to the scalar degrees of freedom responsible for the spectator sector phase transition, baryogenesis requires CP-violating interactions beyond those of the Standard Model. In the present work, these effects have been parameterized by the same effective higher-dimensional operator and the benchmark scale $\Lambda = 1$ TeV used in Ref. [47]. We have not attempted to construct a complete ultraviolet realization of this operator. Other CP-violating operators, as well as additional interactions between the spectator sector and the Standard Model, could modify the baryon yield and may open regions of parameter space in which a larger asymmetry is obtained. Exploring these possibilities in explicit particle-physics realizations is an important direction for future work.

The same PBH population also gives rise to GW signals over widely separated frequency ranges. Direct Hawking emission of gravitons provides a generic high frequency contribution, while an additional signal induced by PBH density fluctuations can arise if the PBH abundance is sufficiently large to generate an intermediate PBH dominated epoch before evaporation [51, 53]. These two signals probe different aspects of the PBH population and provide complementary signatures of the inflationary spectator sector dynamics.

In the present analysis, the GW signal induced by PBH density fluctuations has been evaluated using the monochromatic approximation. The finite duration of the nucleation process, however, generically gives rise to a PBH mass distribution with a nonzero width, even when the distribution is sufficiently narrow for a monochromatic treatment to provide a useful leading approximation. Recent work has shown that a finite-width mass distribution of evaporating PBHs can suppress the induced GW signal relative to the idealized

monochromatic case, owing to the continuous depletion of PBHs with different evaporation times [90–93]. Such a suppression could relax the corresponding GW restriction on the PBH abundance. However, in the PBH dominated regime the baryon yield need not increase proportionally with the PBH abundance because the accompanying entropy injection also becomes larger. A quantitative assessment therefore requires a joint treatment of the extended PBH mass distribution, its evaporation and entropy-production history, the baryogenesis window, and the resulting GW spectrum. We leave such an analysis for future work.

A more complete treatment would require solving the time-dependent bubble wall dynamics, including the evolution of the vacuum pressure throughout the inflationary feature, together with a more precise determination of the supercritical bubble evolution, the resulting PBH mass distribution, and its subsequent evaporation history. On the baryogenesis side, it would be particularly valuable to study the hydrodynamic explosion and electroweak transport together with explicit ultraviolet completions of the CP-violating operators. These developments would allow a more precise determination of the PBH abundance, the final baryon asymmetry, and the associated GW signals. Nevertheless, the present analysis demonstrates that a single spectator sector phase transition during inflation can consistently connect vacuum bubble nucleation, PBH formation, Hawking evaporation, baryogenesis, and GW production, providing a framework in which these phenomena can be studied within a common cosmological history.

Acknowledgments

This work is supported by the National Natural Science Foundation of China (NNSFC) Grant No. 12475111 and the Fundamental Research Funds for the Central Universities, Sun Yat-sen University.

A Vacuum Decay and Stability at the End of Inflation

This appendix collects the technical details of the vacuum decay calculation used in Sec. 2. We first give the explicit mapping of the spectator potential to the semi-analytic de Sitter tunneling fit of Ref. [56]. We then rewrite the potential at the end of inflation in a shifted field basis in which the nonzero metastable vacuum is located at the origin, and use this form to estimate its decay both before and after reheating. The post-reheating decay is treated as a zero-temperature $O(4)$ process using the quartic-potential fit of Ref. [65].

A.1 CDL tunneling during inflation

At fixed N, the spectator potential can be written in the form used in Ref. [56],

$$U_N(s) = \frac{1}{2} m^2_{\rm SST} s^2 - \mu_{3,\rm SST} s^3 + \lambda_{4,\rm SST} s^4, \tag{A.1}$$

with

$$m^2_{\rm SST}(N) = m^2(N), \qquad \mu_{3,\rm SST} = \frac{b}{3}, \qquad \lambda_{4,\rm SST} = \frac{\kappa}{4}. \tag{A.2}$$

The corresponding dimensionless variables are

$$\varepsilon_{\rm SST}(N) = \delta_N, \tag{A.3}$$

$$\mathcal{H}_{\rm SST}(N) = \frac{H_i}{m_{\rm deg}\sqrt{1-\delta_N}}, \tag{A.4}$$

and

$$\Omega_{\rm SST}(N) = \sqrt{\varepsilon^2_{\rm SST}(N) + \mathcal{H}^2_{\rm SST}(N)}. \tag{A.5}$$

The CDL tunneling exponent is then

$$B^{\rm SST}_{\rm CDL}(N) = \frac{\pi^2}{6\kappa}(1-\delta_N)\widetilde{B}_{\rm SST}\left[\varepsilon_{\rm SST}(N), \Omega_{\rm SST}(N)\right]. \tag{A.6}$$

For completeness, the fitting function used in the numerical calculation is

$$\begin{aligned}\widetilde{B}_{\rm SST}(\varepsilon,\Omega) = {} & \frac{4\left(1+10.07\varepsilon+16.55\varepsilon^2\right)}{\Omega(\varepsilon+\Omega)^2(1+10\varepsilon)} \\ & \times\left[1+\frac{11}{2}\varepsilon+\frac{3\varepsilon^2}{\Omega}+\frac{3\varepsilon^3}{2\Omega^2}\right]\widetilde{B}_2(\varepsilon,\Omega),\end{aligned} \tag{A.7}$$

where

$$\widetilde{B}_2(\varepsilon,\Omega) = 1 + \sum_{i,j} k_{ij}\varepsilon^i\Omega^j, \tag{A.8}$$

with nonzero coefficients

$$\begin{aligned} &k_{01} = -0.1617, && k_{03} = -5.507, && \\ &k_{11} = -11.34, && k_{12} = 30.17, && k_{14} = -21.69, \\ &k_{20} = 12.09, && k_{21} = -33.24, && k_{23} = 41.29, \\ &k_{30} = 7.728, && k_{32} = -19.34. && \end{aligned} \tag{A.9}$$

The characteristic tunneling exponent associated with the nucleation rate concentrated around $N_\star$ is

$$B_\star \equiv B^{\rm SST}_{\rm CDL}(N_\star). \tag{A.10}$$

Neglecting gravitational backreaction in the SST treatment requires

$$\kappa_{\rm SST}(N) \equiv \frac{8\pi G\, m^4_{\rm SST}(N)}{\mu^2_{3,\rm SST}} = \frac{32\pi G b^2}{9\kappa^2}(1-\delta_N)^2. \tag{A.11}$$

At the characteristic nucleation point, we therefore require

$$\kappa_{{\rm SST},\star} \ll \min\left\{1,\, \max\left(\mathcal{H}_{{\rm SST},\star}, \varepsilon_{{\rm SST},\star}\right)\right\}. \tag{A.12}$$

The magnitude of the curvature at the barrier top is

$$\mu^2_{\rm top}(N) \equiv -U''_N(s_{-,N}) = \frac{b^2}{18\kappa}q_N(3-q_N). \tag{A.13}$$

Within the quasi-static, weak-backreaction quartic treatment, we impose

$$\frac{\mu_{\mathrm{top},\star}^2}{H_i^2} \gtrsim 4 \tag{A.14}$$

to select the nonconstant CDL branch rather than the broad Hawking–Moss regime [56]. This condition is used as a branch-selection criterion within the present quartic approximation and should not be interpreted as a general criterion for an arbitrary scalar potential.

A.2 Shifted Potential at the End of Inflation

At the end of inflation, the $s = 0$ configuration is the true vacuum, whereas the nonzero minimum is a positive energy metastable state. We define

$$q_{\mathrm{end}} \equiv \sqrt{1 + 8\delta_{\mathrm{end}}}, \qquad 0 < q_{\mathrm{end}} < 1, \tag{A.15}$$

so that

$$s_{+,\mathrm{end}} = \frac{b}{6\kappa}(3 + q_{\mathrm{end}}). \tag{A.16}$$

To describe tunneling from this metastable state, it is convenient to shift the field according to

$$\varphi \equiv s_{+,\mathrm{end}} - s. \tag{A.17}$$

The metastable vacuum is then located at $\varphi = 0$, while the true vacuum $s = 0$ corresponds to

$$\varphi_{\mathrm{tv}} = s_{+,\mathrm{end}} = \frac{b}{6\kappa}(3 + q_{\mathrm{end}}). \tag{A.18}$$

Subtracting the metastable vacuum energy, we define

$$\Delta U_{\mathrm{in}}(\varphi) \equiv U_{\mathrm{end}}\left(s_{+,\mathrm{end}} - \varphi\right) - U_{\mathrm{end}}\left(s_{+,\mathrm{end}}\right). \tag{A.19}$$

Using the stationarity condition for $s_{+,\mathrm{end}}$, the shifted potential takes the form

$$\Delta U_{\mathrm{in}}(\varphi) = \frac{\kappa}{4}\varphi^4 - \frac{b}{6}(1 + q_{\mathrm{end}})\varphi^3 + \frac{b^2}{36\kappa} q_{\mathrm{end}}(3 + q_{\mathrm{end}})\varphi^2. \tag{A.20}$$

The barrier top in the shifted variable is

$$\varphi_{\mathrm{top}} = s_{+,\mathrm{end}} - s_{-,\mathrm{end}} = \frac{b}{3\kappa} q_{\mathrm{end}}. \tag{A.21}$$

Eq. (A.20) is the potential used below to estimate the lifetime of the metastable bubble interior.

A.3 Vacuum Decay before Reheating

Before instantaneous reheating, the metastable state present at the end of inflation is embedded in the inflationary de Sitter background. Its decay can therefore be estimated using the same semi-analytic de Sitter tunneling description introduced above, provided that the corresponding nonconstant bounce solution exists.

Matching Eq. (A.20) to

$$\Delta U_{\rm in}(\varphi) = \frac{1}{2} m^2_{\rm SST,end}\varphi^2 - \mu_{3,\rm end}\varphi^3 + \lambda_{4,\rm end}\varphi^4 \tag{A.22}$$

gives

$$m^2_{\rm SST,end} = \frac{b^2}{18\kappa} q_{\rm end}(3+q_{\rm end}), \tag{A.23}$$

and

$$\mu_{3,\rm end} = \frac{b}{6}(1+q_{\rm end}), \qquad \lambda_{4,\rm end} = \frac{\kappa}{4}. \tag{A.24}$$

The corresponding SST variables are

$$\varepsilon_{\rm SST,end} = \frac{1-q_{\rm end}}{(1+q_{\rm end})^2}, \tag{A.25}$$

$$\mathcal{H}_{\rm SST,end} = \frac{H_i}{m_{\rm SST,end}}, \qquad \Omega_{\rm SST,end} = \sqrt{\varepsilon^2_{\rm SST,end} + \mathcal{H}^2_{\rm SST,end}}. \tag{A.26}$$

When the nonconstant CDL branch is applicable, the corresponding exponent is

$$B^{\rm SST}_{\rm CDL,end} = \frac{\pi^2}{6\kappa}\frac{q_{\rm end}(3+q_{\rm end})}{(1+q_{\rm end})^2}\widetilde{B}_{\rm SST}\left(\varepsilon_{\rm SST,end}, \Omega_{\rm SST,end}\right). \tag{A.27}$$

The gravitational-backreaction parameter associated with the potential at the end of inflation is

$$\kappa_{\rm SST,end} \equiv \frac{8\pi G m^4_{\rm SST,end}}{\mu^2_{3,\rm end}} = \frac{8\pi G b^2}{9\kappa^2}\frac{q^2_{\rm end}(3+q_{\rm end})^2}{(1+q_{\rm end})^2}. \tag{A.28}$$

Accordingly, Eq. (A.27) is used only when

$$\kappa_{\rm SST,end} \ll \min\left\{1,\, \max\left(\mathcal{H}_{\rm SST,end}, \varepsilon_{\rm SST,end}\right)\right\}. \tag{A.29}$$

For a sufficiently broad barrier, the relevant de Sitter transition is instead described by the Hawking–Moss saddle. From Eq. (A.20), the barrier height above the metastable vacuum is

$$\Delta U_{\rm top,end} = \frac{b^4}{324\kappa^3} q^3_{\rm end}. \tag{A.30}$$

In the spectator-subdominant limit,

$$\Delta U_{\rm top,end} \ll 3M^2_{\rm Pl}H^2_i, \tag{A.31}$$

the Hawking–Moss action difference can be expanded as

$$B_{\rm HM,end} \simeq \frac{8\pi^2}{3H^4_i}\Delta U_{\rm top,end}, \tag{A.32}$$

which gives

$$B_{\rm HM,end} \simeq \frac{2\pi^2}{243}\frac{b^4}{\kappa^3 H^4_i} q^3_{\rm end}. \tag{A.33}$$

The magnitude of the curvature at the barrier top at the end of inflation is

$$\mu^2_{\rm top,end} = \frac{b^2}{18\kappa} q_{\rm end}(3 - q_{\rm end}). \tag{A.34}$$

For the benchmark treatment adopted here, we use

$$B^{\rm dS}_{\rm end} = \begin{cases} B^{\rm SST}_{\rm CDL,end}, & \dfrac{\mu^2_{\rm top,end}}{H_i^2} > 4, \\ B_{\rm HM,end}, & \dfrac{\mu^2_{\rm top,end}}{H_i^2} \leq 4. \end{cases} \tag{A.35}$$

The CDL expression is used only when Eq. (A.29) is also satisfied. Near the boundary $\mu^2_{\rm top,end}/H_i^2 \simeq 4$, the piecewise prescription should be regarded as an approximate branch selection; a numerical Euclidean calculation would be required for a more precise treatment.

We require the physically relevant de Sitter transition at the end of inflation to be exponentially more suppressed than the bubble nucleation process responsible for the PBH source,

$$B^{\rm dS}_{\rm end} > B_\star + \Delta B_{\rm safe}, \qquad \Delta B_{\rm safe} \gg 1. \tag{A.36}$$

This is an exponent-level benchmark condition rather than a calculation of the full integrated decay probability during the remaining inflationary evolution.

A.4 Post-reheating zero temperature bounce

After reheating, we assume that the spectator sector remains sufficiently decoupled from the ambient radiation bath that thermal corrections to Eq. (A.20) are negligible. The decay of the metastable bubble interior can then be treated as a zero-temperature $O(4)$ tunneling process.

To apply the quartic-potential fit of Ref. [65], we write

$$V_A(\varphi) = \lambda_A \varphi^4 - a_A \varphi^3 + b_A \varphi^2. \tag{A.37}$$

Comparison with Eq. (A.20) gives

$$\lambda_A = \frac{\kappa}{4}, \qquad a_A = \frac{b}{6}(1 + q_{\rm end}), \tag{A.38}$$

and

$$b_A = \frac{b^2}{36\kappa} q_{\rm end}(3 + q_{\rm end}). \tag{A.39}$$

The corresponding shape parameter is

$$D_{\rm A,end} \equiv \frac{8\lambda_A b_A}{a_A^2} = \frac{2q_{\rm end}(3 + q_{\rm end})}{(1 + q_{\rm end})^2}. \tag{A.40}$$

Since $0 < q_{\rm end} < 1$, one has

$$0 < D_{\rm A,end} < 2, \tag{A.41}$$

with $D_{\rm A,end} \to 2$ corresponding to the nearly degenerate thin-wall limit.

The zero-temperature bounce exponent is then

$$B_{4,\mathrm{end}}^{\mathrm{flat}} = \frac{4\pi^2}{3\kappa}(2 - D_{\mathrm{A,end}})^{-3}\left(13.832 D_{\mathrm{A,end}} - 10.819 D_{\mathrm{A,end}}^2 + 2.0765 D_{\mathrm{A,end}}^3\right). \tag{A.42}$$

The post-reheating decay of the metastable bubble interior takes place in a time-dependent cosmological background, so that the corresponding semiclassical tunneling action need not coincide with its flat-space value. As discussed in Ref. [94], the importance of the background evolution can be assessed by comparing the characteristic scale of the tunneling process with the dynamical scales of the FLRW geometry. When the tunneling scale is much shorter than both the Hubble time and the time scale over which the expansion rate changes, the Minkowski-space result provides a good approximation. If these scales become comparable, the tunneling process can become sensitive to the time dependence of the background and the corresponding action can receive appreciable corrections. In particular, sufficiently large bubbles can retain sensitivity to the preceding evolution of the scale factor, including details of the reheating history [94].

The characteristic length entering this comparison depends on the structure of the bounce. In the thick-wall regime, there is no parametrically large separation between the microscopic wall scale and the characteristic size of the bounce configuration, so that the inverse curvature scale at the barrier top provides a useful order-of-magnitude proxy [95–97]. Toward the thin-wall regime, however, the nucleation radius can become parametrically larger than this local microscopic scale. Consequently, a condition based only on the barrier curvature does not by itself establish the validity of the flat-space approximation for a near-thin-wall bounce.

In the present phenomenological analysis, we nevertheless impose a minimal local consistency requirement based on the microscopic curvature scale,

$$R_{b,\mathrm{end}} \sim \left[-\Delta U_{\mathrm{in}}''\left(\varphi_{\mathrm{top}}\right)\right]^{-1/2} = \left[\frac{b^2}{18\kappa} q_{\mathrm{end}}(3 - q_{\mathrm{end}})\right]^{-1/2}, \tag{A.43}$$

and require

$$H_i R_{b,\mathrm{end}} \ll 1. \tag{A.44}$$

This condition ensures that the microscopic scale associated with the barrier is well separated from the cosmological scale immediately after reheating, but it does not exclude configurations whose full nucleation radius becomes larger in the thin-wall regime. We therefore retain such configurations within the present benchmark treatment, while interpreting the corresponding flat-space decay estimate with this limitation in mind. A definitive calculation in this regime would require the detailed reheating history and a solution of the tunneling problem in the resulting time-dependent background, which we leave for future work.

Finally, we require the zero-temperature vacuum decay after reheating to be exponentially more suppressed than the vacuum tunneling process responsible for bubble production,

$$B_{4,\mathrm{end}}^{\mathrm{flat}} > B_\star + \Delta B_{\mathrm{safe}}, \qquad \Delta B_{\mathrm{safe}} \gg 1. \tag{A.45}$$

Together, Eqs. (A.36) and (A.45) provide the benchmark stability conditions adopted in our analysis for the metastable vacuum present at the end of inflation. These conditions are intended as conservative criteria at the level of the tunneling exponent and do not replace a fully time-dependent calculation of the integrated decay probability.

B Spectator Potential Parameters for the Benchmark Points

For completeness, we collect in Table 2 the spectator potential parameters corresponding to the benchmark points presented in Table 1. These quantities specify the microscopic spectator sector realization underlying each benchmark, while the PBH, baryogenesis, and GW quantities reported in Table 1 are derived from the subsequent tunneling, bubble, and cosmological evolution.

The precise value of σ_N is tied to the detailed time-dependent bubble wall dynamics, since it controls the duration over which the relative vacuum energies evolve and therefore affects both the acceleration and the subsequent deceleration of the wall. A self-consistent determination of σ_N would require solving the wall equation of motion throughout the interval over which the spectator potential evolves.

The value of σ_N can also influence the width of the bubble population in scale space. A broader feature in the spectator potential generally allows vacuum tunneling to remain relevant over a wider interval in N, which can in turn broaden the range $\Delta N_{\rm PBH}$ entering the PBH mass distribution and therefore affect the accuracy of the monochromatic approximation. Nevertheless, the relation is not one-to-one, since the nucleation rate depends exponentially on the bounce action, $\Gamma(N) \propto \exp[-B_{\rm CDL}(N)]$. Consequently, a smooth potential feature with a finite width can still generate a much more sharply localized nucleation history when the bounce action develops a sufficiently pronounced minimum, as explicitly illustrated in Ref. [34]. The validity of the monochromatic approximation is therefore controlled directly by the resulting nucleation interval $\Delta N_{\rm PBH}$ rather than by σ_N alone.

The requirement of a small residual wall velocity at the end of inflation may likewise select a non-negligible duration for the wall evolution. In particular, a sufficiently extended post-reversal stage can allow the outward motion acquired near nucleation to be gradually reduced before the end of inflation, rather than requiring an abrupt stopping of the wall. Such a possibility is compatible with a sizable accumulated propagation and hence with a non-negligible $v_{\rm eff}$.

Importantly, the spectator potential contains additional freedom to adjust the relative strength of the driving and decelerating stages. For fixed $N_\star$ and σ_N, the vacuum structure near the nucleation epoch and at the end of inflation is characterized by

$$\delta_\star = 1 - \alpha_0 + \delta_m, \qquad \delta_{\rm end} = 1 - \alpha_0 + \delta_m \exp\left[-\frac{N_\star^2}{2\sigma_N^2}\right]. \tag{B.1}$$

The independent parameters α_0 and δ_m therefore provide freedom to vary the vacuum energy splitting around nucleation and the residual metastable vacuum energy near the

Table 2: Spectator potential parameters corresponding to the benchmark points listed in Table 1. The first five points correspond to $v_{\rm eff} = 0.3$, while the remaining five correspond to $v_{\rm eff} = 0.7$. Since the precise value of σ_N depends on the assumed bubble wall dynamics, we retain parameter sets that remain viable for multiple values of σ_N and do not list it separately.

BP	$v_{\rm eff}$	H_i [GeV]	b [GeV]	κ	α_0	δ_m
BP1	0.3	1×10^{13}	1.189×10^{15}	0.4171	1.001	0.8746
BP2	0.3	1.083×10^{12}	1.287×10^{14}	0.4171	1.0052	0.8789
BP3	0.3	1×10^{13}	1.189×10^{15}	0.4171	1.001	0.8746
BP4	0.3	1.172×10^{11}	1.34×10^{14}	0.4171	1.0095	0.8831
BP5	0.3	1.083×10^{12}	1.287×10^{14}	0.4171	1.018	0.8916
BP6	0.7	1.083×10^{12}	1.533×10^{15}	1.8	1.0052	0.6498
BP7	0.7	1×10^{13}	9.457×10^{13}	0.0967	1.0052	0.9552
BP8	0.7	1×10^{13}	9.457×10^{13}	0.0967	1.0095	0.9595
BP9	0.7	1×10^{13}	9.097×10^{14}	0.0967	1.001	0.951
BP10	0.7	1.172×10^{11}	1.026×10^{14}	0.0967	1.001	0.951

end of inflation separately, subject to the vacuum-structure and stability conditions imposed in the main text. In particular, one can favor a larger vacuum energy difference during the outward-driven stage, enhancing the early wall propagation, while keeping the post-reversal interior vacuum energy relatively small. The latter corresponds to a weaker inward vacuum-pressure contribution and hence to a more gradual deceleration. Together with the finite duration of the post-reversal stage and the other contributions to the wall dynamics, this provides a plausible parameter regime in which the wall can accumulate a sizable displacement during inflation while its residual velocity becomes small by $t_{\rm end}$. The additional parameters controlling the overall scale and shape of the spectator potential provide further flexibility, although not every choice of σ_N can necessarily be compensated while simultaneously satisfying all tunneling, stability, spectator-subdominance, and supercriticality requirements.

In the present phenomenological treatment, we therefore fix $\Delta N_{\rm nuc} = 1$ as a common benchmark and retain parameter sets for which viable solutions are obtained for multiple values of σ_N. This procedure selects regions of parameter space whose phenomenological viability is less sensitive to the precise value of σ_N, thereby reducing the dependence of our results on the unresolved wall dynamics. We therefore do not list a unique value of σ_N for each benchmark point in Table 2. A dedicated calculation of the time-dependent bubble wall evolution, together with the resulting nucleation width and PBH mass distribution, is left for future work.

The parameters listed in Table 2 should be regarded as the microscopic inputs associated with the displayed benchmark points. The corresponding PBH masses and abundances, baryon yields, and GW observables are derived quantities and are summarized in Table 1.

References

[1] A. Mazumdar and G. White, *Review of cosmic phase transitions: their significance and experimental signatures*, *Rept. Prog. Phys.* **82** (2019) 076901 [1811.01948].

[2] M.B. Hindmarsh, M. Lüben, J. Lumma and M. Pauly, *Phase transitions in the early universe*, *SciPost Phys. Lect. Notes* **24** (2021) 1 [2008.09136].

[3] P. Athron, C. Balázs, A. Fowlie, L. Morris and L. Wu, *Cosmological phase transitions: From perturbative particle physics to gravitational waves*, *Prog. Part. Nucl. Phys.* **135** (2024) 104094 [2305.02357].

[4] X. Wang, F.P. Huang and X. Zhang, *Phase transition dynamics and gravitational wave spectra of strong first-order phase transition in supercooled universe*, *JCAP* **05** (2020) 045 [2003.08892].

[5] A. Katz and A. Riotto, *Baryogenesis and Gravitational Waves from Runaway Bubble Collisions*, *JCAP* **11** (2016) 011 [1608.00583].

[6] H. Mansour and B. Shakya, *Particle production from phase transition bubbles*, *Phys. Rev. D* **111** (2025) 023520 [2308.13070].

[7] B. Shakya, *Aspects of particle production from bubble dynamics at a first order phase transition*, *Phys. Rev. D* **111** (2025) 023521 [2308.16224].

[8] G.F. Giudice, H.M. Lee, A. Pomarol and B. Shakya, *Nonthermal heavy dark matter from a first-order phase transition*, *JHEP* **12** (2024) 190 [2403.03252].

[9] W.-Y. Ai, M. Fairbairn, K. Mimasu and T. You, *Non-thermal production of heavy vector dark matter from relativistic bubble walls*, *JHEP* **05** (2025) 225 [2406.20051].

[10] M. Cataldi, K. Müürsepp and M. Vanvlasselaer, *CP-violation in production of heavy neutrinos from bubble collisions*, *JHEP* **01** (2026) 058 [2506.12123].

[11] Z. Cheng and F.P. Huang, *Dark Matter Production from Bubble Collisions during a First-Order Phase Transition at the End of Inflation*, 2605.03758.

[12] A. Ghoshal and P. Pal, *Cosmic collider gravitational waves sourced by right-handed neutrino production from bubbles: Testing scales of the seesaw mechanism, leptogenesis, and dark matter*, *Phys. Rev. D* **113** (2026) 103035 [2601.02458].

[13] M.Y. Khlopov, R.V. Konoplich, S.G. Rubin and A.S. Sakharov, *Formation of black holes in first order phase transitions*, hep-ph/9807343.

[14] M.Y. Khlopov, R.V. Konoplich, S.G. Rubin and A.S. Sakharov, *First order phase transitions as a source of black holes in the early universe*, *Grav. Cosmol.* **2** (1999) S1 [hep-ph/9912422].

[15] T.H. Jung and T. Okui, *Primordial black holes from bubble collisions during a first-order phase transition*, *Phys. Rev. D* **110** (2024) 115014 [2110.04271].

[16] J. Liu, L. Bian, R.-G. Cai, Z.-K. Guo and S.-J. Wang, *Primordial black hole production during first-order phase transitions*, *Phys. Rev. D* **105** (2022) L021303 [2106.05637].

[17] M. Lewicki, P. Toczek and V. Vaskonen, *Primordial black holes from strong first-order phase transitions*, *JHEP* **09** (2023) 092 [2305.04924].

[18] Y. Gouttenoire and T. Volansky, *Primordial black holes from supercooled phase transitions*, *Phys. Rev. D* **110** (2024) 043514 [2305.04942].

[19] M. Lewicki, P. Toczek and V. Vaskonen, *Black Holes and Gravitational Waves from Slow First-Order Phase Transitions*, *Phys. Rev. Lett.* **133** (2024) 221003 [2402.04158].

[20] S. Kanemura, M. Tanaka and K.-P. Xie, *Primordial black holes from slow phase transitions: a model-building perspective*, *JHEP* **06** (2024) 036 [2404.00646].

[21] K. Murai, K. Sakurai and F. Takahashi, *Primordial black hole formation via inverted bubble collapse*, *JHEP* **07** (2025) 065 [2502.02291].

[22] Z. Ning, X.-X. Zeng, R.-G. Cai and S.-J. Wang, *Numerical simulations of primordial black hole formation via delayed first-order phase transitions*, *JCAP* **07** (2026) 073 [2601.21878].

[23] A.M. Green and B.J. Kavanagh, *Primordial Black Holes as a dark matter candidate*, *J. Phys. G* **48** (2021) 043001 [2007.10722].

[24] B. Carr and F. Kuhnel, *Primordial black holes as dark matter candidates*, *SciPost Phys. Lect. Notes* **48** (2022) 1 [2110.02821].

[25] K. Sato, M. Sasaki, H. Kodama and K.-i. Maeda, *Creation of Wormholes by First Order Phase Transition of a Vacuum in the Early Universe*, *Prog. Theor. Phys.* **65** (1981) 1443.

[26] H. Kodama, M. Sasaki, K. Sato and K.-i. Maeda, *Fate of Wormholes Created by First Order Phase Transition in the Early Universe*, *Prog. Theor. Phys.* **66** (1981) 2052.

[27] H. Kodama, M. Sasaki and K. Sato, *Abundance of Primordial Holes Produced by Cosmological First Order Phase Transition*, *Prog. Theor. Phys.* **68** (1982) 1979.

[28] J. Garriga and A. Vilenkin, *Watchers of the multiverse*, *JCAP* **05** (2013) 037 [1210.7540].

[29] J. Garriga, A. Vilenkin and J. Zhang, *Black holes and the multiverse*, *JCAP* **02** (2016) 064 [1512.01819].

[30] H. Deng and A. Vilenkin, *Primordial black hole formation by vacuum bubbles*, *JCAP* **12** (2017) 044 [1710.02865].

[31] H. Deng, *Primordial black hole formation by vacuum bubbles. Part II*, *JCAP* **09** (2020) 023 [2006.11907].

[32] D.N. Maeso, L. Marzola, M. Raidal, V. Vaskonen and H. Veermäe, *Primordial black holes from spectator field bubbles*, *JCAP* **02** (2022) 017 [2112.01505].

[33] H.-L. Huang and Y.-S. Piao, *Toward supermassive primordial black holes from inflationary bubbles*, *Phys. Rev. D* **110** (2024) 023501 [2312.11982].

[34] H. Wang, Y.-l. Zhang and T. Suyama, *Nearly Monochromatic Primordial Black Holes as total Dark Matter from Bubble Collapse*, 2510.19233.

[35] S.R. Coleman and F. De Luccia, *Gravitational Effects on and of Vacuum Decay*, *Phys. Rev. D* **21** (1980) 3305.

[36] H. Lee and E.J. Weinberg, *Negative modes of Coleman-De Luccia bounces*, *Phys. Rev. D* **90** (2014) 124002 [1408.6547].

[37] S.W. Hawking, *Black hole explosions*, *Nature* **248** (1974) 30.

[38] J.H. MacGibbon and B.J. Carr, *Cosmic rays from primordial black holes*, *Astrophys. J.* **371** (1991) 447.

[39] J. Auffinger, *Primordial black hole constraints with Hawking radiation—A review*, *Prog. Part. Nucl. Phys.* **131** (2023) 104040 [2206.02672].

[40] A. Cheek, L. Heurtier, Y.F. Perez-Gonzalez and J. Turner, *Primordial black hole evaporation and dark matter production. I. Solely Hawking radiation*, *Phys. Rev. D* **105** (2022) 015022 [2107.00013].

[41] L. Morrison, S. Profumo and Y. Yu, *Melanopogenesis: Dark Matter of (almost) any Mass and Baryonic Matter from the Evaporation of Primordial Black Holes weighing a Ton (or less)*, *JCAP* **05** (2019) 005 [1812.10606].

[42] S. Jiang and F.P. Huang, *Pseudo-Goldstone dark matter from primordial black holes: gravitational wave signatures and implications for KM3-230213A event at KM3NeT*, *JCAP* **06** (2025) 023 [2503.14332].

[43] T. Kuwahara and Y. Uchida, *Composite asymmetric dark matter assisted by primordial black holes evaporation*, *Phys. Rev. D* **114** (2026) 055033 [2511.16354].

[44] R. Calabrese, M. Chianese, J. Gunn, G. Miele, S. Morisi and N. Saviano, *Limits on light primordial black holes from high-scale leptogenesis*, *Phys. Rev. D* **107** (2023) 123537 [2305.13369].

[45] J. Gunn, L. Heurtier, Y.F. Perez-Gonzalez and J. Turner, *Primordial black hole hot spots and out-of-equilibrium dynamics*, *JCAP* **02** (2025) 040 [2409.02173].

[46] Y. Chang, S. Tang, H. Deng, Y. Wang, R. Ding and F.P. Huang, *Effects of Early-Universe Inhomogeneity on Bubble Formation: Primordial Black Holes as an Extreme Case*, 2511.11408.

[47] A.P. Klipfel, M. Vanvlasselaer, S. Trifinopoulos and D.I. Kaiser, *Baryogenesis from Exploding Primordial Black Holes*, 2603.29024.

[48] M. Vanvlasselaer, S. Trifinopoulos, A.P. Klipfel and D.I. Kaiser, *Shocks from Exploding Primordial Black Holes in the Early Universe*, 2603.15746.

[49] M. D'Onofrio, K. Rummukainen and A. Tranberg, *Sphaleron Rate in the Minimal Standard Model*, *Phys. Rev. Lett.* **113** (2014) 141602 [1404.3565].

[50] M. Hong, K. Kamada and J. Yokoyama, *Baryogenesis from sphaleron decoupling*, *Phys. Rev. D* **108** (2023) 063502 [2304.13999].

[51] A. Ireland, S. Profumo and J. Scharnhorst, *Primordial gravitational waves from black hole evaporation in standard and nonstandard cosmologies*, *Phys. Rev. D* **107** (2023) 104021 [2302.10188].

[52] A.D. Dolgov and D. Ejlli, *Relic gravitational waves from light primordial black holes*, *Phys. Rev. D* **84** (2011) 024028 [1105.2303].

[53] G. Domènech, C. Lin and M. Sasaki, *Gravitational wave constraints on the primordial black hole dominated early universe*, *JCAP* **04** (2021) 062 [2012.08151].

[54] G. Domènech and J. Tränkle, *From formation to evaporation: Induced gravitational wave probes of the primordial black hole reheating scenario*, *Phys. Rev. D* **111** (2025) 063528 [2409.12125].

[55] D. Borah and N. Das, *Multi-peaked high-frequency gravitational waves from PBH-assisted leptogenesis*, 2606.23787.

[56] M. Sasaki, E.D. Stewart and T. Tanaka, *General solutions for tunneling of scalar fields with quartic potentials in de Sitter space*, *Phys. Rev. D* **50** (1994) 941 [hep-ph/9402247].

[57] P.P. Avelino, C.J.A.P. Martins and L. Sousa, *Dynamics of Biased Domain Walls and the Devaluation Mechanism*, *Phys. Rev. D* **78** (2008) 043521 [0805.4013].

[58] L. Kofman, A.D. Linde, X. Liu, A. Maloney, L. McAllister and E. Silverstein, *Beauty is attractive: Moduli trapping at enhanced symmetry points*, *JHEP* **05** (2004) 030 [hep-th/0403001].

[59] S. Enomoto, S. Iida, N. Maekawa and T. Matsuda, *Beauty is more attractive: particle production and moduli trapping with higher dimensional interaction*, *JHEP* **01** (2014) 141 [1310.4751].

[60] S. Kikuchi, T. Kobayashi, K. Nasu and Y. Yamada, *Moduli trapping mechanism in modular flavor symmetric models*, *JHEP* **08** (2023) 081 [2307.13230].

[61] D. Green, B. Horn, L. Senatore and E. Silverstein, *Trapped Inflation*, *Phys. Rev. D* **80** (2009) 063533 [0902.1006].

[62] L. Pearce, M. Peloso and L. Sorbo, *The phenomenology of trapped inflation*, *JCAP* **11** (2016) 058 [1603.08021].

[63] S.R. Coleman, *The Fate of the False Vacuum. 1. Semiclassical Theory*, *Phys. Rev. D* **15** (1977) 2929.

[64] C.G. Callan, Jr. and S.R. Coleman, *The Fate of the False Vacuum. 2. First Quantum Corrections*, *Phys. Rev. D* **16** (1977) 1762.

[65] F.C. Adams, *General solutions for tunneling of scalar fields with quartic potentials*, *Phys. Rev. D* **48** (1993) 2800 [hep-ph/9302321].

[66] S.W. Hawking, *Particle Creation by Black Holes*, *Commun. Math. Phys.* **43** (1975) 199.

[67] D.N. Page, *Particle Emission Rates from a Black Hole: Massless Particles from an Uncharged, Nonrotating Hole*, *Phys. Rev. D* **13** (1976) 198.

[68] D. Hooper, G. Krnjaic and S.D. McDermott, *Dark Radiation and Superheavy Dark Matter from Black Hole Domination*, *JHEP* **08** (2019) 001 [1905.01301].

[69] R.J. Scherrer and M.S. Turner, *Decaying Particles Do Not Heat Up the Universe*, *Phys. Rev. D* **31** (1985) 681.

[70] Particle Data Group collaboration, *Review of particle physics*, *Phys. Rev. D* **110** (2024) 030001.

[71] A. Deur, S.J. Brodsky and G.F. de Teramond, *The QCD Running Coupling*, *Nucl. Phys.* **90** (2016) 1 [1604.08082].

[72] D. Kara, *Corrections of Order $\alpha\alpha_s$ to W Boson Decays*, *Nucl. Phys. B* **877** (2013) 683 [1307.7190].

[73] G.M. Prosperi, M. Raciti and C. Simolo, *On the running coupling constant in QCD*, *Prog. Part. Nucl. Phys.* **58** (2007) 387 [hep-ph/0607209].

[74] A. Mariotti, X. Nagels, A. Rase and M. Vanvlasselaer, *DW-genesis: baryon number from domain wall network collapse*, *JHEP* **03** (2025) 199 [2411.13494].

[75] D. Bodeker and W. Buchmuller, *Baryogenesis from the weak scale to the grand unification scale*, *Rev. Mod. Phys.* **93** (2021) 035004 [2009.07294].

[76] G. Barni, *Electroweak Baryogenesis with BARYONET: a self-contained review of the WKB approach*, *SciPost Phys.* **21** (2026) 032 [2510.21915].

[77] J.R. Espinosa, B. Gripaios, T. Konstandin and F. Riva, *Electroweak Baryogenesis in Non-minimal Composite Higgs Models*, *JCAP* **01** (2012) 012 [1110.2876].

[78] J. van de Vis, J. de Vries and M. Postma, *Bubble trouble: A review on electroweak baryogenesis*, *Prog. Part. Nucl. Phys.* **150** (2026) 104244 [2508.09989].

[79] R. Cooke, M. Pettini, R.A. Jorgenson, M.T. Murphy and C.C. Steidel, *Precision measures of the primordial abundance of deuterium*, *Astrophys. J.* **781** (2014) 31 [1308.3240].

[80] Planck collaboration, *Planck 2015 results. XIII. Cosmological parameters*, *Astron. Astrophys.* **594** (2016) A13 [1502.01589].

[81] C. Pitrou, A. Coc, J.-P. Uzan and E. Vangioni, *Precision big bang nucleosynthesis with improved Helium-4 predictions*, *Phys. Rept.* **754** (2018) 1 [1801.08023].

[82] K. Schmitz, *New Sensitivity Curves for Gravitational-Wave Signals from Cosmological Phase Transitions*, *JHEP* **01** (2021) 097 [2002.04615].

[83] LIGO Scientific collaboration, *Advanced LIGO*, *Class. Quant. Grav.* **32** (2015) 074001 [1411.4547].

[84] M. Punturo et al., *The Einstein Telescope: A third-generation gravitational wave observatory*, *Class. Quant. Grav.* **27** (2010) 194002.

[85] D. Reitze et al., *Cosmic Explorer: The U.S. Contribution to Gravitational-Wave Astronomy beyond LIGO*, *Bull. Am. Astron. Soc.* **51** (2019) 035 [1907.04833].

[86] N. Herman, L. Lehoucq and A. Fúzfa, *Electromagnetic antennas for the resonant detection of the stochastic gravitational wave background*, *Phys. Rev. D* **108** (2023) 124009 [2203.15668].

[87] Y. He, S.K. Giri, R. Sharma, S. Mtchedlidze and I. Georgiev, *Inverse Gertsenshtein effect as a probe of high-frequency gravitational waves*, *JCAP* **05** (2024) 051 [2312.17636].

[88] N. Aggarwal et al., *Challenges and opportunities of gravitational-wave searches above 10 kHz*, *Living Rev. Rel.* **28** (2025) 10 [2501.11723].

[89] C. Caprini and D.G. Figueroa, *Cosmological backgrounds of gravitational waves*, *Class. Quant. Grav.* **35** (2018) 163001 [1801.04268].

[90] X.-C. He, X.-H. Ma, M. Sasaki and V. Takhistov, *Universal Suppression of Gravitational Waves from Black Hole Evaporation Dynamics*, 2606.09804.

[91] K. Inomata, M. Kawasaki, K. Mukaida, T. Terada and T.T. Yanagida, *Gravitational Wave Production right after a Primordial Black Hole Evaporation*, *Phys. Rev. D* **101** (2020) 123533 [2003.10455].

[92] T. Papanikolaou, *Gravitational waves induced from primordial black hole fluctuations: the effect of an extended mass function*, *JCAP* **10** (2022) 089 [2207.11041].

[93] Y. Gouttenoire, N. Leister and P. Schwaller, *Gravitational Waves from Black Hole Reheating: The Scalar-Induced Component*, 2605.21474.

[94] D. Simon, J. Adamek, A. Rakic and J.C. Niemeyer, *Tunneling and propagation of vacuum bubbles on dynamical backgrounds*, *JCAP* **11** (2009) 008 [0908.2757].

[95] A. Mégevand and F.A. Membiela, *Thin and thick bubble walls. Part I. Vacuum phase transitions*, *JCAP* **06** (2023) 007 [2302.13349].

[96] H. Widyan, A. Mukherjee, N. Panchapakesan and R.P. Saxena, *Bubble formation in phi**4 theory in the thin wall limit and beyond*, hep-th/9803089.

[97] T. Hayashi, K. Kamada, N. Oshita and J. Yokoyama, *On catalyzed vacuum decay around a radiating black hole and the crisis of the electroweak vacuum*, *JHEP* **08** (2020) 088 [2005.12808].